Journal of Electron Spectroscopy and Related Phenomena 227 (2018) 51–68

Contents lists available at ScienceDirect

Journal of Electron Spectroscopy and Related Phenomena

journal homepage: www.elsevier.com/locate/elspec

The influence of internal and external electric fields on the transport of energetic electrons in nanostructures

Mario Marpe[a], Andreas Wucher[a], Detlef Diesing[b,*]

[a] Faculty of Physics, University of Duisburg-Essen, 47048 Duisburg, Germany
[b] Institute of Physical Chemistry, Faculty of Chemistry, University of Duisburg Essen, 45117 Essen, Germany

ARTICLE INFO

Keywords:
SEM
MIM
Metal–insulator–metal
Electron irradiation
Yield
Thin-film
External electron emission
Internal electron emission
Impact angle dependence
Bias

ABSTRACT

Sandwich like metal–insulator–metal (MIM) nanostructures consisting of a 50 nm silver film and a 30 nm aluminum film separated by a few nanometer aluminum oxide layer were irradiated with a focused e-beam (diameter 0.5 mm) at kinetic impact energies in the range of 100 eV to 1000 eV. To distinguish between *internal* transport of hot charge carriers across the buried insulator (tunnel junction) and parasitic electron transport mediated by *externally* emitted electrons re-entering the sample, an additional "dome" electrode was implemented which was biased to positive or negative potential in order to establish an external accelerating or retarding field above the nanostructure's surface. Different device currents induced by the primary electron irradiation were measured either by metering the irradiated or non-irradiated electrode, respectively. The dependence of the detected device currents on impact parameters such as the irradiated position on the MIM surface, the kinetic energy and impact angle of the primary electrons was studied. These experiments were accomplished while changing the internal electric field by an *internal* bias voltage between the top and the bottom electrode of the MIM and while changing the external electric field by applying a voltage to the dome electrode. The measured currents are interpreted in terms of *external* and *internal* emission yields. It is shown that the external electric field allows a clear discrimination between true *internal* electron transport and *external* electron transport leaving the MIM nanostructure on one site and re-entering at another site. The results demonstrate that "internal" currents measured without an external dome electrode may be strongly influenced or even falsified by such cross-absorption effects.

1. Introduction

Kinetic electron beam induced electron emission from solid samples is the basis for the image forming process in **s**canning **e**lectron **m**icroscope (SEM) [1]. The electrons being re-emitted from the sample are conventionally classified in so-called (i) secondary electrons with an energy lower than 50 eV and (ii) back scattered electrons with energies above 50 eV up to the energy of the primary electron beam E_{prim} [2]. The secondary electrons can also be used for the image formation process in a SEM by acceleration mediated by a grid electrode and subsequent detection in a scintillation process [3].

Kinetic ion beams are known to produce also so-called internal electronic excitations inside an irradiated solid [4–7]. These internal excitations are evoked by the deceleration of projectiles inside the solid. The energy transfer to the target's electron gas during this stopping process is surprisingly high even for low kinetic energies $E < 10$ keV [8].

These normally hidden internal electronic excitation processes in the bulk of a silver film was studied by thin film metal–insulator–metal (MIM) nanostructures via monitoring the internal electron emission over the only several nm thin insulator barrier [9]. This internal emission process was later on used to characterize a multitude of electronic excitations induced for example by (i) chemical surface reactions [10] (ii) photo excitation [11,12] (iii) two photon photo illumination [13] or (iv) Auger disexcitation of highly ionized ions [14,15]. MIM devices offer also the unique possibility to detect excited electrons as well as excited holes. The selection of the detection mode is realized by the application of a bias voltage between the two metals [16]. Despite the variety of experiments, a careful study comparing the internal electron emission over the insulator barrier with the external electron emission over the metal's surface barrier was missing.

Recently, a first comparison of internal and external electron emission was made by irradiating MIM devices with a focused electron beam at impact energies between 100 eV and 1000 eV [17]. It could be

* Corresponding author.
E-mail address: detlef.diesing@uni-due.de (D. Diesing).

https://doi.org/10.1016/j.elspec.2018.07.002
Received 16 April 2018; Accepted 12 July 2018
Available online 01 August 2018

proven that the impact of the primary electron beam leads to a measurable device current between the two metal electrodes in addition to that current generated by *external* electron emission into the vacuum, but the partitioning between *internal* and *external* emission processes could not be uniquely deduced from the experimental data. In particular, the question remained unanswered whether the measured "*internal*" current was entirely due to hot charge carriers traversing the tunneling junction, or whether it was somehow influenced by *externally* emitted electrons circumventing the *internal* tunnel barrier.

In order to clarify this point and investigate possible issues arising from secondary electron emission when nano electronic devices are studied in a SEM [18], an external electric field was applied to an electron irradiated MIM nanostructure. The MIM nanostructures were produced in a cross configuration with a 30 nm-thick aluminum "bottom" and a 50 nm-thick silver "top" electrode separated by a 3 nm-thick aluminum oxide layer produced by anodic oxidation. The anodic oxidation is a consumptive process leading to an aluminum thickness slightly thinner than 30 nm [19].

In the previous study mentioned above, external and internal emission currents were measured as a function of electron energy and impact point of the electron beam on the MIM structure [17]. In addition, an internal electric field was generated across the oxide film by applying a bias voltage of up to ± 1 V between the top silver and the aluminum bottom electrode. It was found that the e-beam induced internal device current was surprisingly large and moreover practically independent of the primary electron energy and impact angle. From these results, it was suspected that external electron emission may have to be included in the interpretation of apparently internal transport currents measured in such a device, and the addition of an external electric field was suggested in order to address this question. The experiments presented here therefore represent a continuation of that work. An additional electrode above the irradiated sample surface was added in order to generate such an external field and investigate its influence on the measured device currents. The polarity of the field is either chosen such as to accelerate secondary electrons away from the irradiated surface, as in the conventional Everhart-Thornley [3] setup, or the field is used with opposite polarity to repel the secondary electrons back to the sample. By this method it is possible to manipulate and control the external emission process allowing to study its influence on the measured internal device current.

2. Experiment

2.1. Setup

100 eV to 1000 eV electrons impinging on the several 10 nm thick electrodes of a metal–insulator–metal sandwich system will in part be elastically reflected (in the following referred to as "**back-scattered electrons**" or BSE) and partly cause an emission of low-energy secondary electrons (in the following referred to as "**secondary electrons**" or SE). Both processes generate a current of electrons which are emitted back from the irradiated surface area into the vacuum. In this work, an additional halfpipe-like "**dome electrode**" set to a variable potential produces a defined external electric field above the irradiated sample.

Depending on the voltage U_d applied between the dome electrode and the irradiated surface, this external electrode can either act as collector or as a repeller for beam induced electrons leaving the sample.Experiments have shown that values of $U_d = \approx \pm 40$ V are sufficient to completely repel or collect the externally emitted low energy secondary electrons, respectively (as shown later in Fig. 11). A slit of ≈ 4 mm width in the dome electrode allows the focused primary electron beam (diameter of ≈0.5 mm) to travel unobstructed to the sample. The current of electrons back reflected to the dome electrode can be measured, thereby permitting experiments similar to the usual electron spectroscopy setup with an external collector. The currents into the different electrodes of the irradiated MIM device are measured

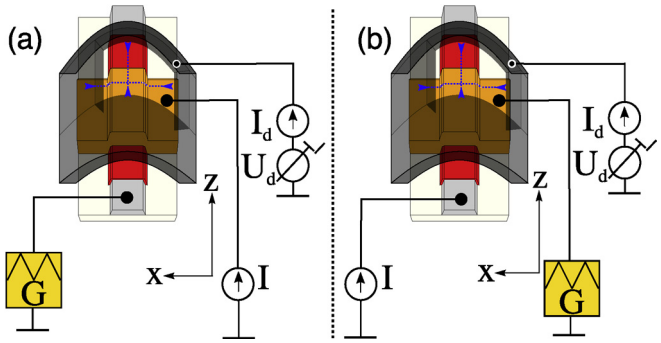

Fig. 1. Schematic of the set-up: (a) *probe top* mode where the current into the silver top electrode (orange) is measured while keeping the aluminum bottom electrode (light gray) at a constant potential. Silver and aluminum are separated by a 4 nm thick oxide layer (red). The dome electrode (dark gray) is kept at U_d while metering the current I_d to the dome. The sample is either moved horizontally in *x*-direction or vertically in *z*-direction as symbolized by the blue dashed lines while detecting all currents as a function of the momentary beam position. (b) **probe bottom** mode where the current into the aluminum bottom electrode is measured and the silver top electrode is kept at a constant potential. (For interpretation of the references to color in this figure legend, the reader is referred to the web version of this article.)

using the current-monitoring input of a potentiostat (Heka PG 510). If the current into the top silver or bottom aluminum electrode of the MIM is measured, the experiment mode is called "**probe top**" or "**probe bottom**", respectively. In both modes, the electrode which is not metered is connected to the "counter electrode" terminal (marked with the character G for generator in 1) of the potentiostat and kept at a constant potential, usually at 0 V with respect to the other MIM electrode unless a bias voltage is applied.

Depending on the position of the impact point on the MIM device and the measurement mode (*probe top* or *probe bottom*), two different experimental scenarios are possible (see also the table in Fig. 2):

- In case that the current into the electrode that is irradiated by the primary electron beam is read out, this is called a **direct experiment** and the measured currents are assigned as I_{dir}.
- In case that the current in the non-irradiated electrode is read out by the current meter, this is called an **indirect experiment** and the measured currents are assigned as I_{indir}.

Since U_d was limited to ± 40 V in this work, predominantly low energy SE emitted from the irradiated surface with a maximum kinetic energy of about 50 eV [20] are influenced by this voltage. Backscattered electrons, which mostly undergo only one quasi-elastic interaction in close vicinity to the surface causing only a relatively small energy loss, will be influenced to a much smaller extent. For the highest kinetic impact energies used in this experiment ($E_{kin} \leq 1000$ eV), the influence of the dome voltage on the flux of backscattered electrons can therefore safely be neglected. For both polarities of U_d, these backscattered electrons may therefore hit the dome electrode and can thereby produce a flux of tertiary electrons, which is again composed of BSE and SE. In the case of a negative dome voltage, the low energy SE are accelerated towards the sample and held back otherwise. As a consequence, the measured currents I_{dir} and I_{indir} will be influenced by the polarity of the dome voltage. In case of $U_d > 0$ V, the superscript "+" is used and "−" otherwise, leading to four different measured current values I^+_{dir}, I^-_{dir}, I^+_{indir} and I^-_{indir}, respectively.

All currents were measured as a function of the geometrical impact point of the primary electron beam on the MIM device as sketched in Fig. 2. The location of the impact point is characterized by *(x,z)* coordinates, where the *x*-direction is aligned parallel to the top silver electrode strip and the curved shape of the dome electrode (see Fig. 1). The dome electrode is therefore sketched as a section of an ellipsoid in

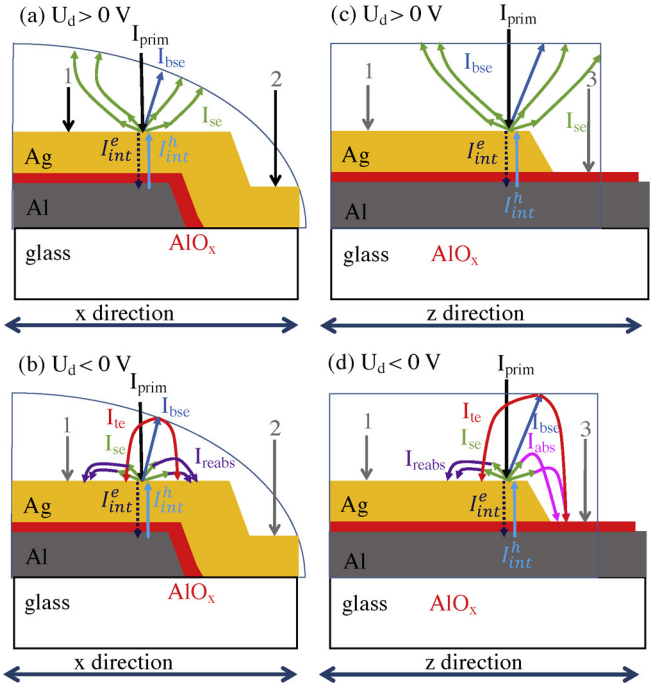

irradiated position	direct experiment	indirect experiment
1	probe top	probe bottom
2	probe top	probe bottom
3	probe bottom	probe top

Fig. 2. Schematic of the irradiation scenarios and the resulting currents: (a) resulting current contributions in *x*-scans for dome voltage $U_d > 0$ V; (b) like (a) for $U_d < 0$ V; (c) for *z*-scans with $U_d > 0$ V; (d) like (c) for $U_d < 0$ V.

panels (a) and (b) of Fig. 2. The *z*-direction is perpendicular to *x* and aligned parallel to the aluminum bottom electrode strip as well as the center axis of the dome electrode, so that the dome electrode is therefore sketched as a horizontal line in panels (c) and (d) of the figure. In order to investigate the dependence of the measured currents on the impact point location, scans with the primary electron beam were performed along the *x*- or *z*-direction, while the other beam coordinate was kept fixed.

2.2. Assignment of current contributions

The different contributions to the measured currents I^{+}_{dir}, I^{+}_{indir}, I^{-}_{dir} and I^{-}_{indir} are sketched in Fig. 2 and assigned as follows:

- I_{prim}: **p**rimary **e**lectron current measured using a Faraday cup
- I_{se}: current caused by **s**econdary **e**lectrons
- I_{bse}: current caused by **b**acks**s**cattered **e**lectrons
- I^{e}_{int}: current caused by **int**ernal emission via **e**lectrons transported across the oxide layer
- I^{h}_{int}: current caused by **int**ernal emission via defect electrons (**h**oles) transported across the oxide layer
- I_{reabs}: current caused by **re-abs**orption of secondary electrons externally leaving and re-entering the irradiated electrode.
- I_{abs}: current caused by secondary or tertiary electrons **abs**orbed in the non-irradiated electrode. This current can in part be caused by (i) **cross-absorbed** secondary electrons leaving the irradiated electrode which are guided back to the sample (by their own electric field on the surface) and enter the non-irradiated electrode and (ii) tertiary electrons being released in the dome electrode by backscattered electrons, leaving the dome surface and ending up in the non-irradiated electrode.
- I_{tde}: current caused by **t**ertiary **d**ome **e**lectrons emitted from the dome electrode and accelerated towards the sample.
- I_{dome}: current measured at the dome electrode.

In addition, we will use the following definitions in the subsequent part of this paper:

- δ: secondary electron emission coefficient, i.e. the average number of secondary electrons released from the irradiated surface per impinging primary electron.
- η: backscattering coefficient, i.e., the average number of primary electrons backscattered from the irradiated surface per impinging primary electron.
- ζ: total emission yield at the irradiated surface with $\zeta = \eta + \delta$.

All currents have by convention a positive sign for electrons entering the monitored electrode and a negative sign for electrons leaving that electrode.

2.3. Measured currents

In this section, all currents which can be measured in the respective experiment are discussed and their contribution to the re-absorption and cross-absorption currents are presented.

In case of a **direct** experiment, where the irradiated electrode is metered, the measured current consists of these contributions:

$$I_{dir} = I_{prim} - I_{int} - I_{se} - I_{bse} + I_{tde} + I_{reabs} \quad (1)$$

In **indirect** experiments, where the non-irradiated electrode is metered, the measured current consists of the following contributions:

$$I_{indir} = I_{int} + I_{abs} \quad (2)$$

where the total internal current crossing the oxide layer is given by the electron and hole contribution:

$$I_{int} = I^{e}_{int} - I^{h}_{int} \quad (3)$$

which, normalized to the primary electron current, defines the internal emission yield

$$\Gamma_{int} = \frac{I}{I_{prim}} \quad (4)$$

In formulating Eqs. (1) and (2), the approximation was made that the entire current of tertiary electrons leaving the dome electrode is measured into the irradiated electrode. This assumption is not well justified, since backscattered electrons may in principle hit the dome electrode everywhere, thereby generating a source of low energy tertiary electrons at this point. These electrons then leave the dome surface with a quasi-isotropic angular distribution and may therefore impinge anywhere on the sample or sample holder. Therefore, part of these electrons may enter either the irradiated or the non-irradiated electrode of the MIM device, the first contributing to I_{dir} and the second contributing to I_{indir}, and the partition between both contributions will depend on the location of their emission spot at the dome electrode as well as the electric field between dome and sample. The current measured onto the dome electrode consists of the following contribution:

$$I_{dome} = I_{se} + I_{bse} - I_{tde} \quad (5)$$

If a voltage U_d is applied between the dome electrode and the sample, the measured currents are changed as follows:

For $U_d > 0$, externally emitted electrons are drained towards the dome and the emission of tertiary electrons from the dome towards the sample becomes suppressed. For sufficiently large values of U_d, this leads to a complete extraction of all emitted electrons, corresponding to

$$I_{reabs} = 0, \quad I_{abs} = 0 \quad \text{and} \quad I_{tde} = 0 \quad (6)$$

Under these conditions, the **direct** current (Eq. (1)) simplifies to

$$I^{+}_{\mathrm{dir}} = I_{\mathrm{prim}} - I_{\mathrm{int}} - I_{\mathrm{se}} - I_{\mathrm{bse}} \tag{7}$$

and the **indirect** current (Eq. (2)) reduces to

$$I^{+}_{\mathrm{indir}} = I_{\mathrm{int}} \tag{8}$$

Normalizing these currents to the primary electron current yields

$$\frac{I^{+}_{\mathrm{dir}}}{I_{\mathrm{prim}}} = 1 - \gamma_{\mathrm{int}} - \delta + \eta = 1 - \gamma_{\mathrm{int}} - \zeta \tag{9}$$

$$(9)\&(4) \Rightarrow \boxed{1 - \frac{I^{+}_{\mathrm{dir}}}{I_{\mathrm{prim}}} - \frac{I^{+}_{\mathrm{indir}}}{I_{\mathrm{prim}}} = \zeta} \tag{10}$$

The current measured at the dome electrode is given by the equation

$$(5) \Rightarrow \boxed{I^{+}_{\mathrm{dome}} = I_{\mathrm{se}} + I_{\mathrm{bse}} = \zeta \cdot I_{\mathrm{prim}}} \tag{11}$$

since the emission of tertiary dome electrons is inhibited due to the dome's electrical field.

For $U_{\mathrm{d}} < 0$, externally emitted electrons are reflected towards the sample and contribute to the re- and cross-absorption currents. For sufficiently negative values of U_{d}, all emitted secondary electrons are kept back at the sample surface, yielding

$$I_{\mathrm{se}} = I_{\mathrm{reabs}} + I_{\mathrm{abs}} \tag{12}$$

At the same time, all tertiary electrons emitted from the dome electrode are now accelerated towards the sample. The **direct** current measured under these conditions is

$$I^{-}_{\mathrm{dir}} = I_{\mathrm{prim}} - I_{\mathrm{int}} - I_{\mathrm{se}} - I_{\mathrm{bse}} + I_{\mathrm{tde}} + I_{\mathrm{reabs}} \tag{13}$$

and the **indirect** current (Eq. (2)) by

$$I^{-}_{\mathrm{indir}} = I_{\mathrm{int}} + I_{\mathrm{abs}} \tag{14}$$

Summing (13) and (14) results in

$$\Rightarrow I^{-}_{\mathrm{dir}} + I^{-}_{\mathrm{indir}} = I_{\mathrm{prim}} - I_{\mathrm{bse}} + I_{\mathrm{tde}} \tag{15}$$

$$\Rightarrow \boxed{1 - \frac{I^{-}_{\mathrm{dir}}}{I_{\mathrm{prim}}} - \frac{I^{-}_{\mathrm{indir}}}{I_{\mathrm{prim}}} = \eta \cdot (1 - \delta_{\mathrm{dome}})} \tag{16}$$

Note that the partition of I_{tde} between I_{dir} and I_{indir} is irrelevant in Eq. (16), where δ_{dome} denotes the low energy electron emission coefficient at the dome electrode surface. The current measured at the dome electrode is given by the equation

$$(5) \Rightarrow I^{-}_{\mathrm{dome}} = I_{\mathrm{bse}} - I_{\mathrm{tde}} \tag{17}$$

since the secondary electrons emitted from the sample are reflected and therefore do not reach the dome.

Concerning the stability of the samples and the repeatability of the measurements, current-voltage characteristics of the MIM device were recorded frequently between different experiments to verify that the sample characteristics remained unchanged. The current of the electron beam as well as its focal properties were measured before and after each experiment, and the measurements were repeated if a discrepancy between the current before and after the measurements was above 5%. The primary electron beam diameter was in all cases about 0.75 mm. Before and after each experiment, the primary electron current of the e-beam was measured with the FC.

2.4. Sample characterization

The metal–insulator–metal sandwich systems used as samples were prepared in the same way as discussed in detail elsewhere [17]. They consist of an aluminum bottom electrode strip (dimensions $18 \cdot 4\ \mathrm{mm}^2$) evaporated under UHV conditions onto a glass substrate. The aluminum film was anodically oxidized to form a 3 nm-thick AlO_x-film, which represents the insulating tunneling barrier of the MIM device [21–23].

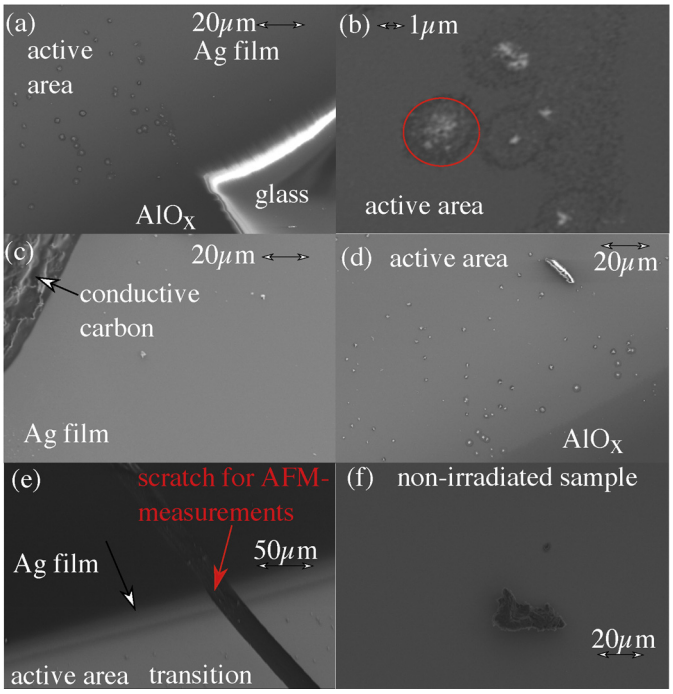

Fig. 3. SEM images of MIM samples (a): overview of the overlap between active area, silver film and the AlO_x film and the glass substrate showing visible contamination where the sample was frequently irradiated. (b): zoom image of the active area: Typical diameter of the contamination is 2 µm. (c): image of the silver film next to the active area where the sample was rarely irradiated: nearly flat surface with a low amount of contamination. (d): image of the active area where the sample was frequently irradiated, a rod like dust particle and small circular structures are visible. (e): image of the boundary between active area/silver film of an irradiated sample; a needle scratch made intentionally for AFM thickness measurements is visible. (f): image of the silver film of a non-irradiated sample showing dust flakes but no circular structures.

The top electrode was fabricated by evaporating a silver film strip of $10 \cdot 4\ \mathrm{mm}^2$ dimension across the aluminum/AlO_x film. The thickness of the silver film was about 50 nm, that of the aluminum film about 30 nm (including the 3 nm-thick AlO_x-film) as reported in [17]. The edges of the aluminum film and the silver film are influenced by the shadows of evaporation masks in the vacuum chamber. Due to the shadow of the evaporation mask, both metal films run out at the edge over a distance of some 10 µm [11]. Since the e-beam diameter is of ≈0.5 mm, the edges cannot be resolved by the electron beam. The so-called "active area" of the MIM device is the region where all three layers overlap and the tunneling junction is formed; its dimension is about $4 \cdot 4\ \mathrm{mm}^2$. The dynamic capacitance C_{d} of the resulting device is found to be practically identical to the one reported before [17].

In our previous experiments the measured currents showed a peculiar behavior when irradiating a particular spot in the center of the active area [17]. This behavior was tentatively attributed to a carbon contamination of the surface, which was assumed to be generated by prolonged electron irradiation. To support this interpretation, a comparison of irradiated areas with non-irradiated areas by means of a **S**canning **E**lectron **M**icroscope SEM was performed. The resulting SEM images are shown in Fig. 3. Panel (a) shows an image of the irradiated part of the sample. Small circular structures are clearly visible on the surface of the active area as well as on the silver film outside the active area. The bright light-up at the edges of the metal film is induced by charging the surface of the glass substrate during the scanning process in the SEM. A temporal evolution of the brightness is observed during the scans.

A zoom with a larger magnification is shown in panel (b). The diameter of the circular structures (circled in red) can be estimated to

be ≈2 µm. In panel (c), a non irradiated part of the silver film is shown with smaller magnification, but no circular structures appear on this image. This means that the circular structures seen in panels (a) and (b) are clearly induced by the e-beam. In panel (c), only few flakes are visible, which are pieces of dust that show up on all parts of the sample. This can hardly be avoided since the samples are not prepared in a clean-room environment. In panel (d), an irradiated part of the silver film within the active area is shown, recorded with the smaller magnification, also showing small circular structures as discussed above. In panel (e), the transition of the active area towards the silver film on the glass substrate is shown. The transition visible in form of a gradient in grey scale has a width of about 50 µm, which is caused by the wedge-shaped coast-down of the aluminum film on the edges.

A scratch through the sample is also visible, which was deliberately fabricated by a needle to enable the measurement of the film thicknesses by means of an **a**tomic **f**orce **m**icroscope (AFM). In panel (f), an image of a non-irradiated sample is shown. Although dust flakes (size > 10 µm) are visible on the silver film of the sample, no contamination like in panel (d) is observable. This also proves that the circular structures are a direct consequence of the irradiation of the sample with the 100-1000 eV electron-beam. The diameter of the circles (≈2 µm) is far smaller than the beam-diameter of (≈500 µm).

3. Results and discussion

3.1. Methodology of the experiments

In this section, we will present the results of current measurements into the top silver or bottom aluminum electrode of the investigated MIM device. All measured current values displayed in the following graphs will be presented as normalized to the primary electron current measured using the Faraday cup. During most of the experiments, no bias voltage was applied between the two MIM electrodes except where especially indicated.

This section is organized as follows:

- *The position dependence* of currents measured for different kinetic electron impact energies at static dome voltages $U_d = -40$ V and at $U_d = +40$ V are presented in Section 3.2 in the following order:
  - Results from *x*-scans obtained in *probe top* and *probe bottom* mode are presented and discussed in Sections 3.2.1 and 3.2.4.
  - Results from *z*-scans are presented in Section 3.2.5 and the position-dependence is separated into *direct* and *indirect* experiments depending on the exact position in the scan.
  - The experiments for constant U_d and variable position are discussed in terms of different current contributions to the measured signals in Section 3.3.
  - The *impact angle dependence* of the measured currents is discussed in Section 3.4.
- *The dome voltage dependence* of the measured current is presented and discussed in Section 3.5 for irradiation on a static position within the active area in the *probe top* and the *probe bottom* modes, representing *direct* as well as *indirect* experiments.
  - *Direct* experiments are shown in Section 3.5.2 and their impact energy dependence for $U_d = -40$ V, for $U_d = 0$ V and for $U_d = +40$ V is extracted.
  - *Indirect* experiments at a static position and variable U_d are presented for different kinetic energies and discussed in Section 3.5.2 and the energy dependence for $U_d = -40$ *V*, for $U_d = 0$ *V* and for $U_d = +40$ *V* is extracted.
  - The total yield ζ is determined from *direct* experiments at static position and variable U_d and the results are compared to literature data in Section 3.6.
  - *The bias voltage dependence* of the current measured in *probe bottom* mode is presented and discussed in Section 3.7.

3.2. Position dependent current measurements

As shown in Fig. 2, the impact point of the e-beam – in connection with the current measuring mode (*probe top* or *probe bottom*) influences the nature of the experiments (*direct* vs. *indirect*).

(i) Irradiation on positions 1 and 2 (located on the silver film *within* and *outside* the active area, respectively) along with a current measurement in *probe top* mode represents a *direct* experiment, since the current into the irradiated electrode is monitored. The same applies to irradiation on position 3 (located on the aluminum film on top of the glass) and measurement in *probe bottom* mode.

(ii) Irradiation on the positions 1 and 2 (silver film) along with a current measurement in the *probe bottom* mode and irradiation on position 3 (aluminum electrode) along with a current measurement in the *probe top* mode constitute *indirect* experiments, where the current monitoring electrode is different from the irradiated electrode. Therefore, during a *z*-scan from position 1 to position 3 (see Fig. 2) the nature of the experiment changes from *direct* to *indirect* in *probe top* mode and vice versa in *probe bottom* mode. Examples of such experiments are discussed in Section 3.2.5. In contrast, the nature of the experiment does not change during *x*-scans from position 1 to position 2 (see Fig. 2), which are discussed in Sections 3.2.1 and 3.2.4. More specifically, the experiment remains *indirect* in *probe bottom* mode and *direct* in *probe top* mode throughout the entire scan. This means that *x*- and *z*-scans need to be analyzed differently depending on the irradiation scenario.

3.2.1. x-scans – finding the active area on the sample

The *x*-coordinates of the active area are identical with the *x*-coordinates of the aluminum electrode, since the oxidized aluminum electrode forms the basis of the active MIM junction. The precise determination of these *x*-coordinates is important for the further interpretation of the scan experiment. For this reason an *x*-scan with a path located partly on the glass substrate and partly on the oxidized aluminum electrode was performed as shown in pictogram (1) of Fig. 4. The constant *z*-coordinate during this scan was $z = 149.5$ mm, corresponding to a position located about 1 mm away from the edge of the silver film. The results of the scan performed along this path are compared with an *x*-scan performed at $z = 147.3$ mm, where the scanning path is located well within the silver film (see pictogram 2 in Fig. 4).

3.2.2. x-scans – probe bottom experiments (black lines in Fig. 4)

When scanning across the aluminum film according to pictogram (1) in Fig. 4, the *x*-positions of the aluminum electrode edges – marking the active area (shimmed in gray) – are obtained by those points where the measured current rises to and decreases from the plateau value ($\frac{I}{I_{prim}} \approx -1.5$) in plot (a1) of Fig. 4, which was measured at a dome voltage U_d of +40 V.

The normalized current is negative, indicating that more electrons leave the surface than impinge onto it. In fact, a normalized current value of −1.5 indicates a total emission yield $\zeta = 2.5$, meaning that on average 2.5 electrons leave the surface per impinging primary electron. The appearance of strong secondary emission from oxide covered surfaces is discussed in the literature as Malter effect [24] and is commonly explained by the reduced work function due to the presence of the thin oxide layer on top of the bottom aluminum film [25]. The *x*-coordinates representing the edges of the aluminum electrode are 34.7 mm and 39 mm, respectively. The interstice, depicting the *x*-extension of the active area defined by the overlap of top silver and bottom aluminum electrodes, is marked as grey box in this and the following figures. Thus, for $x < 34.7$ mm and $x > 39$ mm the e-beam hits the glass substrate in this particular scan.

During irradiation of the glass, the electrons interact with a good insulator with a band gap of ≈8 eV [26]. This value is valid for bulk samples but decreases to ≈3 eV in a thin oxide film due to the influence

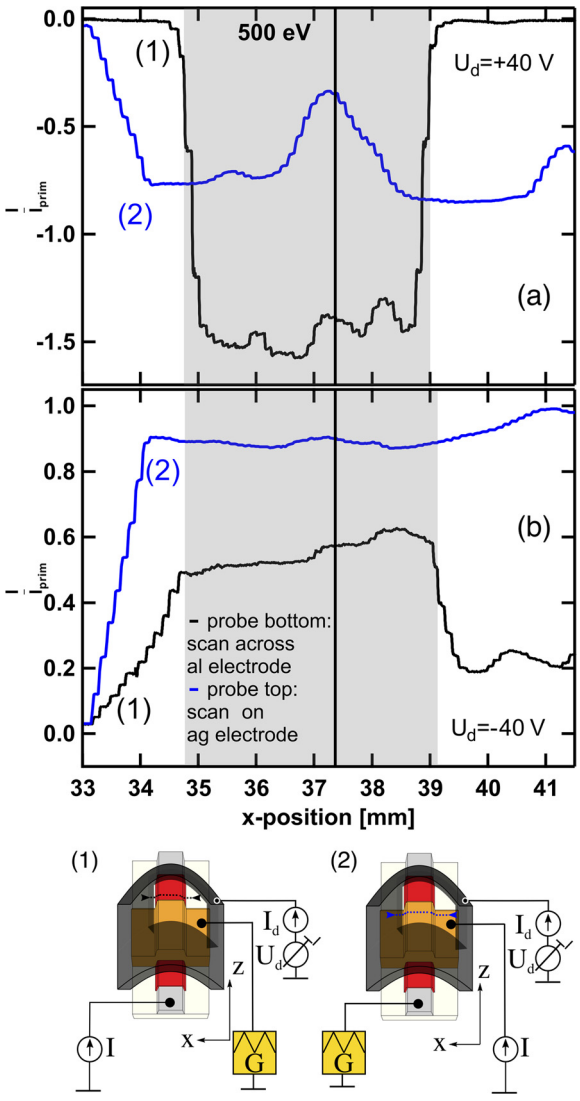

Fig. 4. *Upper graph*, $U_d = +40$ V: (1) Normalized current measured in the bottom aluminum electrode as a function of the *x*-position during a scan of the primary electron beam across the aluminum electrode (see pictogram (1)). (2) Normalized current measured in the silver top electrode as a function of the *x*-position for scanning across the silver electrode (see pictogram (2)). *Lower graph*, $U_d = -40$ V: Methodology for (1) and (2) is the same. In both graphs the black line indicates the *x*-position where the *z*-scans (see Section 3.2.5) were performed. (For interpretation of the references to color in this figure legend, the reader is referred to the web version of this article.)

of the metal oxide interfaces [27]. Since the energy of the impinging electrons is at least 10 times higher than the band gap and, hence, the work function of the glass, electron bombardment may cause the emission of secondary electrons from the glass surface. If the total emission yield ζ is below unity, the surface of the insulator will quickly become negatively charged up to the primary electron energy, thereby preventing further electron bombardment of this spot. In case of $\zeta > 1$, on the other hand, the glass surface will build up a positive charge, which refrains a part of the emitted low energy electrons from leaving the irradiated area. As a consequence, a dynamic equilibrium is established where the impinging and emitted currents just balance, corresponding to zero net current into the glass substrate. Nevertheless, the secondary electrons released from the glass will be influenced by the dome voltage and – depending on the value of U_d – may end up as a measurable current into the nearby aluminum electrode. In case of a positive dome voltage, they are drained towards the dome electrode, and the normalized current measured in the aluminum electrode under these conditions is practically zero. A negative dome voltage, on the other hand, deflects the secondary electrons back to the sample and leads to a well detectable positive current into the aluminum electrode (plot (b1) for $x > 39$ mm and $x < 34.7$ mm). The signal rise in the regime $34.3\text{ mm} < x < 34.7\text{ mm}$ is caused by a geometrical shadowing effect, since the dome electrode partly masks the sample and the primary electron beam can only pass to the sample through the entrance slit of the dome electrode. As the beam reaches the aluminum electrode, the signal increases from 0.3 to 0.5, and the normalized current remains positive, since the negative potential of the dome electrode effectively suppresses the secondary electron emission from the aluminum surface. The slight increase from 0.5 to 0.6 while scanning across the aluminum film is probably caused by changes of the suppression effect induced by a slightly changing field geometry, since the irradiated spot moves within the dome electrode slit area. For $x < 39$ mm, the signal decreases again to about 0.2, and the signal observed during the remainder of the scan ($x > 39.5$ mm) is again caused by the release of electrons from the glass substrate.

3.2.3. *x*-scans – probe top experiments (blue lines in Fig. 4)

The linear signal change between $x = 33$ mm and $x = 34$ mm observed in parts (a2) and (b2) of Fig. 4 again reflects the beam shadowing effect discussed above. The measurements performed in the **probe top** mode while irradiating the top silver electrode show no significant position dependence in case of a negative dome voltage (plot (b2) of Fig. 4). Under these conditions, all secondary electrons released from the sample are repelled back to the irradiated surface. In addition, the tertiary electrons generated by the impact of high energy backscattered electrons onto the dome electrode are also accelerated towards the sample, thereby counteracting the effect of the backscattered electron current. Both effects apparently lead to an almost negligible net electron emission from the irradiated surface, yielding a normalized positive current of about 1. For a positive dome voltage, on the other hand, the measured current is negative, corresponding again to a total emission yield larger than unity. The normalized current of about −0.75 (curve a2) measured in the left and right part of the silver film indicates a value of $\zeta = 1.75$. However, a pronounced local maximum is observed when the electron beam hits the center of the silver film at $x = 37.3$ mm, which had also been observed in our previous study [17]. As described therein and discussed in Section 2.4, we attribute this feature to a local carbon contamination of the surfaces, which is generated due to prolonged electron bombardment in this area. The argument for this interpretation is that the feature is found at the particular *x*-position where all *z*-scans were performed (marked by the black solid line in the figure at $x = 37.3$ mm). Therefore, this particular location at the device surface was irradiated during every single measurement performed in this work and has therefore received by far the largest primary electron fluence. It is known that a carbon contamination changes the surface work function, leading to a pronounced change in the secondary electron emission coefficient. Consequently, the normalized current of about −0.45 measured at this spot reflects a reduced value of $\zeta = 1.45$ as compared to 1.75 for the clean silver surface.

3.2.4. Energy dependence of *x*-scans

In Fig. 5, results from *x*-scans measured at different kinetic electron impact energies are shown. As before, the grey box marks the width and position of the underlying aluminum film.

- In panel (a) of Fig. 5, the measurements performed in *probe top* mode with $U_d = +40$ V are shown, where all secondary electrons are drained to the dome and no tertiary electrons leave the dome towards the sample. From $x = 33$ mm to 34 mm, one finds again the linear change of the signal due to the masking effect of the dome electrode slit. When the electron beam passes the dome electrode

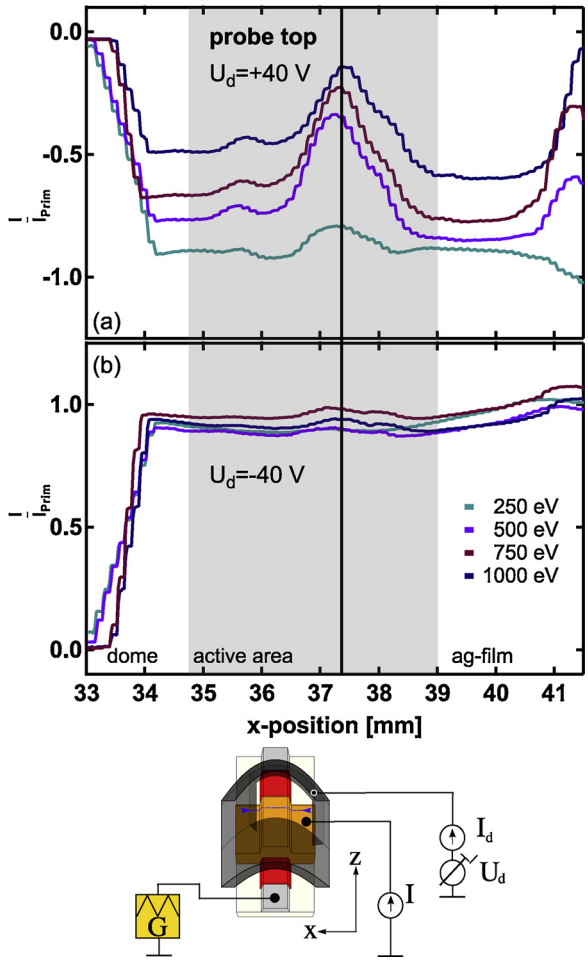

Fig. 5. (a): Current in the *probe top* mode measured in the silver electrode normalized to the primary current as function of the *x*-position scanning across the active area for $U_d = +40$ V. The black line indicates the *x*-position at which the *z*-scans were performed. (b): Like in (a) but with $U_d = -40$ V.

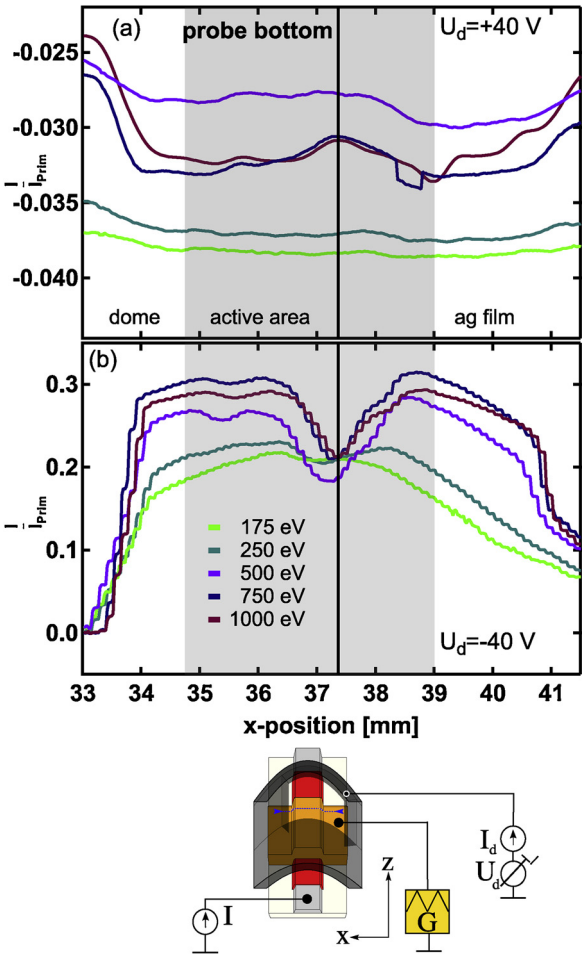

Fig. 6. (a): Current in the *probe bottom* mode measured in the aluminum electrode normalized to the primary current as function of the *x*-position scanning across the active area for $U_d = +40$ V for different kinetic energies. The black line indicates the *x*-position at which the *z*-scans were performed. (b): Like in (a) but with $U_d = -40$ V.

and irradiates the silver film ($x > 34$ mm), the position dependence is weak on the first two millimeters but again shows a local maximum at $x = 37.3$ mm, which is again attributed to the local carbon contamination in the center of the active area. From $x = 38.5$ mm to $x = 40.5$ mm the measurement again shows only a weak position dependence, until at $x > 41$ mm the e-beam starts to hit the conductive carbon contacts, thereby generating a smaller secondary electron yield. With increasing kinetic electron impact energy, the signal measured at the local maximum (evoked by carbon contamination) as well as on the clean silver surface part of the active area shows a clear energy dependence. For low kinetic energies the signal increases from -0.9 to -0.45 on the clean silver surface while it increases from -0.85 to -0.2 when the electron beam hits the carbon contamination. As discussed above, the apparent signal increase originates from a reduction of the secondary electron emission coefficient, which is obviously stronger on the carbon contaminated part of the silver surface.

- Panel (b) of Fig. 5 shows the measurements performed with a negative dome voltage, where electron emission from the irradiated surface is largely suppressed. These measurements again show the linear increase from $x = 33$ mm to 34 mm due to the shadowing effect of the dome electrode slit. When the e^- fully hits the silver film, the measured current shows neither a position nor an energy dependence. The carbon contaminated area at $x \approx 37.3$ mm also does not seem to play a special role in this case. Under these conditions, the effective secondary electron emission yield ζ is close to zero, leading to $I \approx I_{prim}$ for all energies and positions as discussed above.

In Fig. 6, results from *x*-scans measured in *probe bottom* mode are plotted for different kinetic electron impact energies. Since the silver top electrode is irradiated and the current is measured in the aluminum bottom electrode, these measurements have to interpreted as *indirect* experiments. Panel (a) of Fig. 6 shows the measurements recorded at a positive dome voltage. At first sight, it is obvious that negative values of the normalized currents are observed, indicating a net flow of negative charge from the bottom aluminum to the top silver electrode. If electrons would simply penetrate the top silver film and traverse the oxide layer into the bottom electrode, the current would be counted with a positive sign. The measured negative current can therefore either be caused by the internal emission of electrons from the bottom, not irradiated aluminum electrode into the top silver electrode (which appears unlikely to happen), or the effective current is predominantly caused by defect electrons (holes) traversing the oxide layer from the top silver to the bottom aluminum electrode. Another important observation is the relatively small magnitude of the observed internal emission current in panel (a) as compared to all measured currents discussed above.

Despite these small absolute values a clear impact energy dependence is visible. Because the experiment is *indirect*, along with the

influence of the electric field induced by the dome electrode, the current measured at positive dome voltage must be interpreted as a true internal emission current through the oxide barrier of the MIM, because the cross-absorption of external electrons leaving the irradiated silver surface and the absorption of tertiary electrons emitted from the dome electrode is suppressed in this case. In judging the nature of the measured current, one should keep in mind that both excited electrons and holes may contribute to the internal emission current with opposite sign. Therefore, both contributions counteract and can in principle also completely cancel each other, leading to a measured effective current of zero. In fact, such a zero crossing and even a sign change of the measured internal current has previously been observed in MIM experiments where the bias voltage between the two electrodes was varied, thereby modifying the balance between electron and hole currents [28] (see also Section 3.7). In that context, it is interesting to note that the negative current is also measured when irradiating the sample outside the active area. It is already observed at the beginning of the scan at $x = 33$ mm, where the beam does not even impinge onto the MIM device but hits the dome electrode instead. Since a negative current into the aluminum electrode cannot be induced by an absorption of electrons released anywhere in the system, we attribute this "background" signal – which also shows a clear impact energy dependence – to the irradiation of the (oxidized) aluminum electrode from the wings of the primary electron beam. The negative sign then again corresponds to the large electron emission yield of that electrode as discussed above. At $x = 34$ mm, the beam reaches the slit in the dome electrode and impinges onto the silver electrode outside of the active area. This transition is accompanied by an increase of the measured negative current and ranges from about -0.038 at 175 eV to -0.032 at 1000 eV. The lowest value of -0.028 appears for 500 eV electron energy. This current is the true internal current across the MIM tunneling junction, which are obviously observed whenever the silver electrode is irradiated, regardless of the irradiated spot being located within (grey area) or outside of the active area.

Panel (b) of Fig. 6 shows the results recorded at a negative dome voltage. In contrast to the data presented in panel (a), the measured current is in this case positive and of much larger magnitude, indicating a significant net transport of negative charge into the aluminum electrode. A signal change in the region of the carbon contamination with a prominent local minimum at $x = 37.2$ mm emphasizes a close connection of these experiments with the measurements performed in the *probe top* mode, which showed a local maximum at the same z-position at positive U_d (see panel (a) of Fig. 5). The typical signal increase between $x = 33$ mm and 34 mm due to the dome slit shadowing effect appears also here. The feature observed in the carbon contamination region has also the usual width of ≈ 1 mm. With a more detailed comparison between the data presented in panel (b) of Fig. 6 and in panels (a) of Figs. 4 and 5, one finds that

- the carbon contamination reduces the effective emission current into the aluminum bottom electrode in comparison to the clean silver surface. This is similar to the carbon contamination induced reduction of the external electron emission from the silver top electrode into the vacuum as visible in panels (a) of Figs. 4 and 5.
- the effective emission current into the aluminum bottom electrode measured under irradiation of the carbon contaminated spot shows only a weak impact energy dependence, whereas that measured under irradiation of the clean silver surface shows a strong energy dependence (as visible in panel (b) of Fig. 6 at $x \approx 37.3$ mm and for example at $x \approx 35.5$ mm).
- the effective emission current into the aluminum bottom electrode increases with increasing impact energy from ≈ 0.18 at 175 eV electrons to 0.31 at 750 eV electrons (according to an analysis of the data in panel (b) at $x \approx 35.5$ mm). This is the opposite effect to the external electron emission into the vacuum (panel (a) of Fig. 5), where an increase of the electron energy caused a reduction in the total electron emission from the irradiated silver surface.
- The electron emission from the silver top electrode into the vacuum shows a monotonous decrease with increasing electron energy, whereas the effective current into the aluminum bottom electrode shows a maximum at 750 eV energy and decreases again at 1000 eV.

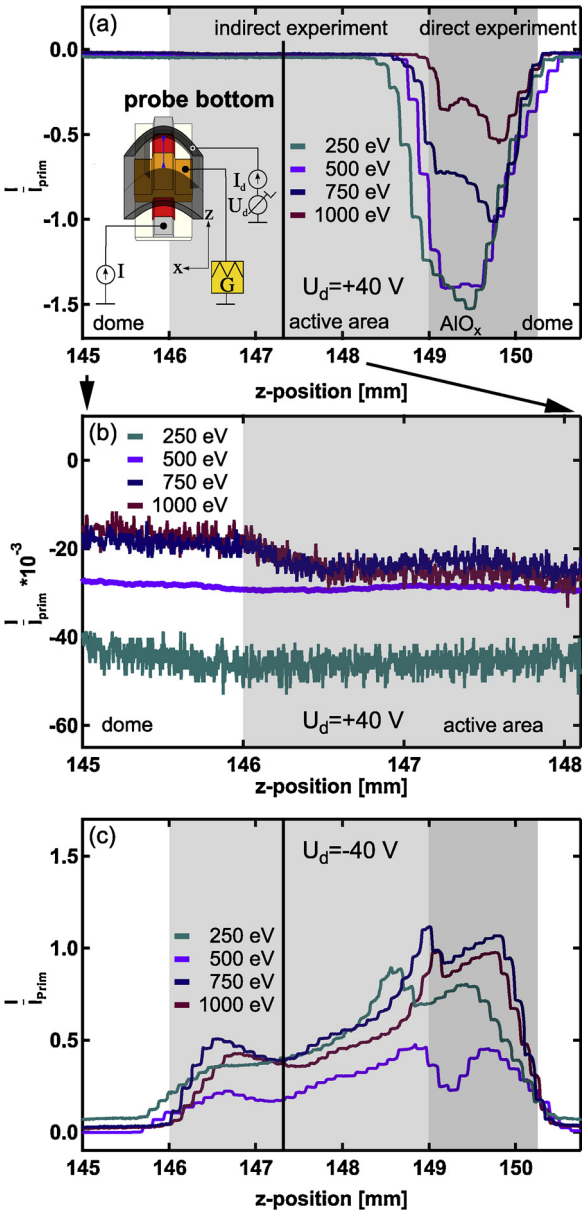

Fig. 7. (a): Normalized current measured in *probe bottom* mode with positive dome voltage $U_d = +40$ V as a function of the z-position while scanning the primary electron beam at different kinetic energies across the active area. (b): Enlarged view of panel (a) for 145 mm $\leq z \leq$ 148 mm. (c): Same as (a) but for $U_d = -40$ V. The black line at $z \approx 147.2$ mm in panels (a) and (c) indicates the z-position at which the x-scans were performed.

A detailed conclusive discussion of these results together with those of the in z-scans presented in Section 3.2.5 will be given in Section 4.

3.2.5. *z-scans*

The z-scans have been performed at $x = 37.5$ mm, i.e., along the center of the aluminum bottom electrode. The results measured in the *probe top* mode are not shown since they do not reveal new findings. The results measured in *probe bottom* mode are shown in Fig. 7, where the data measured at positive and negative dome potential are

displayed in panels (a) and (c), respectively. At the beginning of the scan ($z = 145$ mm), the e-beam still hits the dome electrode and starts to irradiate the silver electrode around $z = 146$ mm. From $z = 146$ mm to $z = 149$ mm, the active area is irradiated. Since the current measuring electrode is the aluminum bottom electrode, the data measured in this z-interval have to be interpreted as an *indirect* experiment. This regime is marked as a light grey sector in panel (a) of Fig. 7.

At $z \approx 149$ mm the e-beam moves from the active area to the bare oxidized aluminum electrode. The aluminum electrode is irradiated now and simultaneously acts as current measuring electrode. Thus, this is a *direct* experiment (marked as dark grey sector in panel (a)). At $z \approx 149.7$ mm the dome electrode starts again to mask the aluminum electrode.

Panel (b) shows a zoom of panel (a) for $145\text{ mm} < z < 148.2\text{ mm}$. A negative current is measured in this regime, again reflecting a net transport of negative charge away from the aluminum electrode. As already observed in Fig. 6, a negative "background" signal is already measured between 145 and 146 mm where the e-beam hits the dome electrode. As visible in panel (a) of Fig. 6, an increase of this negative current is found when the beam starts to irradiate the active MIM area at $z = 146$ mm. The magnitude of this increase, corresponding to the true internal emission current of the MIM device, is the same as observed in the x-scans depicted in Fig. 6.

Around $z = 149$ mm, the nature of the experiment changes from an *indirect* to a *direct* experiment. The normalized current reaches values of -1.5 for 250 eV electron energy, again revealing the strong electron emission from the oxidized aluminum with approximately 2.5 electrons leaving the electrode surface per impinging primary electron. For higher electron energies, the measured normalized current reduces to 0.5, indicating that the electron emission yield decreases as observed above. The transition appears to start the earlier the lower the electron energy. This energy dependence was not observed in x-scans, therefore it might be caused by slight deflection of the primary electron beam caused by the potential of the dome electrode. Around $z = 149.8$ mm, the beam again starts to impinge onto the dome electrode, and the measured current decays to practically zero again.

Panel (c) shows the current measured for negative dome voltage. Again, one finds the transitions between dome irradiation at $z < 146$ mm and $z > 150$ mm, irradiation of the active area at $146.5\text{ mm} < z < 149$ mm and irradiation of the aluminum electrode at $149\text{ mm} < z < 150$ mm. Comparing panels (a) and (c), the most striking difference is the much higher, positive *indirect* current measured when irradiating the active area, which further increases when measuring the *direct* current while irradiating the aluminum electrode. Both findings are consistent with those found in Fig. 6 (b) and are interpreted in the same way. The general structure of the z-scan at a negative dome voltage is:

- a linear increase of the signal between 146 and 146.5 mm,
- a local minimum at $z \approx 147.3$ mm,
- an increase to maximal values for the *indirect* experiment at z values close to but smaller than 149 mm.

The local minimum shows up at the z-coordinate where the e-beam is in the center of the silver top electrode. At this z-coordinate also all x-scans have been performed, so that the occurrence of a local minimum might also reflect the carbon contamination as discussed above. On the other hand, the finding of a larger effective electron emission current into the aluminum electrode when the irradiated spot on the silver surface is closer to the exposed area of that electrode points to an external carrier transport, where electrons released from the top silver surface are deflected back to the sample and are absorbed by the aluminum electrode. Such a mechanism would also be in line with the results displayed in panel (b) of Fig. 6.

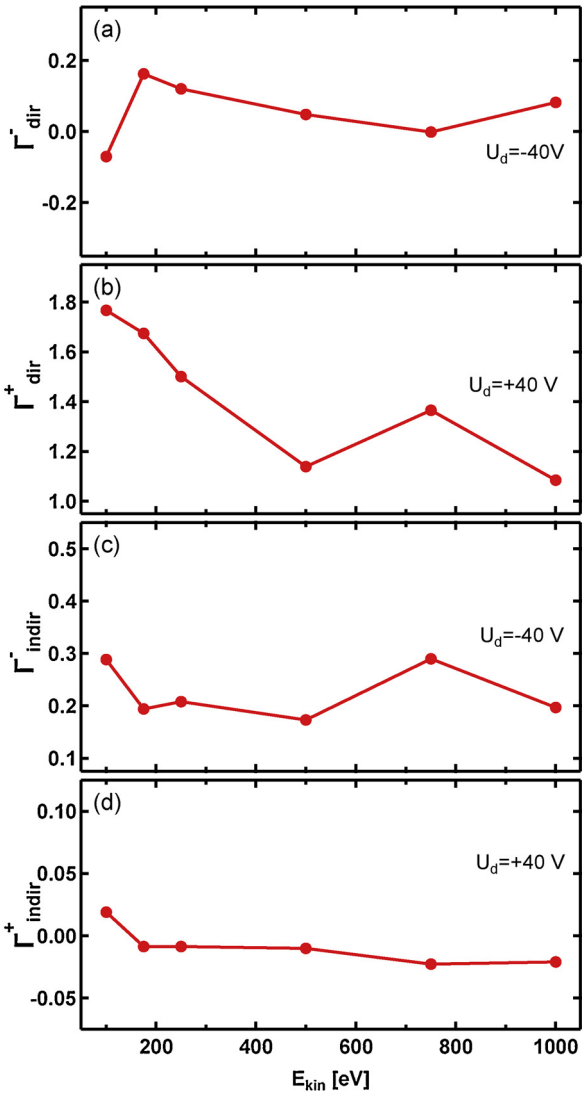

Fig. 8. *Direct* and *indirect* emission yield calculated from the current measured in the irradiated silver electrode (*direct* experiment) (panels (a) and (b)) and the underlying, non-irradiated aluminum electrode (*indirect* experiment) (panels (c) and (d)) measured during irradiation of the active area of a MIM device for positive and negative dome voltages. All current values were normalized to the primary electron current measured using the Faraday cup.

3.3. Evaluation of the current contributions

In this section we analyze the results presented in the previous subsections. We show the energy dependence of the cross-absorption current I_{abs} (in *indirect* measurements), the re-absorption current I_{reabs} (in *direct* experiments), the secondary electron emission current I_{se} and the current of backscattered electrons I_{bse} as defined in Section 2.2. For that purpose, we first summarize the data measured within the active MIM area and show them in Fig. 8. More specifically, we use the measured current I_{dir} and I_{indir} in order to calculate the *direct* and *indirect* emission yields

$$\Gamma_{dir} = 1 - \frac{I}{I_{prim}} \tag{18}$$

$$\Gamma_{indir} = \frac{I}{I_{prim}} \tag{19}$$

The *direct* emission yield Γ_{dir} defined this way describes the net number of negative elementary charges *leaving* the irradiated electrode

per primary electron impact, while Γ_{indir} describes the net number negative elementary charges entering the non-irradiated electrode per primary electron impact. Γ_{dir} and Γ_{indir} will be noted as Γ^{+}_{indir}, Γ^{+}_{dir} for experiments with $+40$ V dome voltage and as Γ^{-}_{indir}, Γ^{-}_{dir} for experiments with -40 V dome voltage.

Panels (a)–(d) show the values of Γ_{dir} and Γ_{indir} measured at positive ($U_d = +40$ V) and negative ($U_d = -40$ V) dome potential as a function of the primary electron impact energy.

The data for Γ^{-}_{dir} depicted in panel (a) show that the current measured in the irradiated silver electrode is about equal to the primary electron current, corresponding to a relatively small net emission of secondary and backscattered electrons away from the irradiated silver surface. This finding is not surprising since the negative dome potential (i) repels low energy secondary electrons back to the sample surface and (ii) pushs tertiary electrons emitted from the dome surface to the sample. The values of Γ^{+}_{dir} measured at positive dome potential, depicted in panel (b) of Fig. 8, show a clear energy dependence. Under these conditions Γ^{+}_{dir} should directly represent the total emission yield ζ of the irradiated surface, indicating $\zeta = 1.8$ and $\zeta = 1.1$ at $E_{prim} = 100$ eV and 1000 eV, respectively.

The *indirect* emission yield Γ^{-}_{indir} measured at negative dome potential is shown in panel (c) of Fig. 8. Apart from statistical scatter, the data show no significant energy dependence. All values are positive and therefore correspond to the transport of negative charge (i.e. electrons) into the underlying aluminum electrode. In principle, this transport may be caused either by (i) an internal electron emission across the MIM tunnel junction or by (ii) a cross-absorption current where externally emitted secondary electrons released from the irradiated silver electrode are deflected back to the sample surface and enter the aluminum electrode outside of the active MIM area. Changing the dome potential now allows to differentiate between these two possibilities.

While the negative value of U_d as used in panel (c) reflects the externally emitted secondary electrons back towards the sample surface, thereby helping to increase both a possible re-absorption or cross-absorption current, a positive value of U_d extracts these electrons away from the sample surface, thereby effectively suppressing both absorption currents I_{reabs} and I_{abs}.

The results obtained with a positive dome voltage are presented in panel (d) of Fig. 8. As already noted above, the *indirect* emission yield measured under these conditions is clearly different from that measured with a negative dome potential. Since external electrons released from the irradiated silver surface are drained toward the dome electrode as in panel (b), the measured current depicted in panel (d) reflects the true internal emission current arising from hot charge carriers generated within the irradiated top silver electrode, which traverse the internal energy barrier formed by the oxide layer and reach the underlying aluminum electrode.

The negative sign of the yield for all impact energies above 100 eV means that negative charge is removed *away* from the aluminum electrode or positive charge is transported into the electrode. As a consequence, the internal emission current must be dominated by the transport of hot holes (defect electrons) across the oxide layer into the aluminum electrode, as already discussed above.

In view of the discussion above, the data presented in panels (c) and (d) of Fig. 8 can be analyzed in terms of the cross-absorption process contribution to the absorption current I_{abs}. This current is of particular interest since it represents a "ghost contribution" to the electron impact induced "device current" measured between the two electrodes of the MIM structure. Evaluating this contribution can therefore help to unravel the different processes underlying the measured device current and determine the true internal emission current across the tunnel junction as discussed above.

At sufficiently high positive dome voltage, the absorption current (cross absorption process) is effectively suppressed, while it fully contributes to the measured device current at sufficiently large negative values of U_d. As outlined above, the current I_{abs} (cross-absorption process, panel (d) in Fig. 2) is thought to be arising from secondary electrons which are externally emitted from the irradiated top electrode surface and are somehow guided back to the sample, thereby hitting the exposed part of the bottom electrode in areas where it is not covered by the top electrode. The results obtained with a varying dome voltage show that this current can be strongly influenced by an external electric field established by the dome electrode.

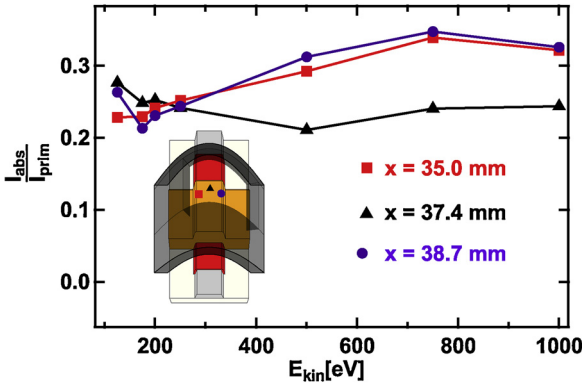

Fig. 9. Cross-absorption yield $\Gamma_{abs} = I_{abs}/I_{prim}$ (Eq. (20) at $U_d = -40$ V), evaluated by Eqs. (8 and 14) measured under irradiation of the top silver surface at the edges of the active MIM junction area ($x = 35.0$, 38.7 mm) and at the position where x-scans and z-scans cross ($x = 37.4$ mm).

As shown in Section 3.5.2, a positive value of $U_d = +40$ V is sufficient to completely suppress this contribution to I_{indir}, while a value of $U_d = -40$ V is sufficient to saturate it. Therefore, we can define a cross-absorption yield Γ_{abs} as

$$\Gamma_{abs} = \frac{I_{abs}}{I_{prim}} \tag{20}$$

where I_{abs} is determined from I^{+}_{indir} and I^{-}_{indir} as defined in Eqs. (8) and (14), respectively, using the data presented in Fig. 8.

The results are shown in Fig. 9 for irradiation of three different spots on the active area. The red squares and the lila circles are the values for Γ_{abs} on the clean silver surface at $x = 35$ mm and at $x = 38.7$ mm on the edges of the active area; the black triangles are the values for the carbon contaminated spot in the center of the active area ($x = 37.4$ mm). The clean and the carbon contaminated surfaces areas show similar values for Γ_{abs} of ≈ 0.25 for $E < 300$ eV. For energies above 300 eV Γ_{abs} on the clean silver surface shows an increase to values above 0.3. For the carbon contaminated area Γ_{abs} decreases when the electron energy is increased from 100 to 500 eV. From 500 eV to 1000 eV a slight increase is monitored, but the carbon contaminated area shows an approximately 20% lower value of Γ_{abs} in this energy range.

3.4. Impact angle dependence

The data shown in Fig. 10 were obtained from x-scans performed at a primary kinetic energy of 500 eV both in the *probe top* and *probe bottom* mode at different impact angles (relative to the surface normal). For the values at a certain angle the x-scans were evaluated by reading out the current values at the x-position of the active area to calculate the *direct* and *indirect* emission yields via Eqs. (18) and (19).

In experiments without external electric field the *direct* emission yield in the topelectrode of MIM systems showed an impact angle dependence, while in *indirect* experiments the yield was found to be largely independent of the impact angle [17]. In panel (a) of Fig. 10, the *direct* emission yield measured for a dome voltage of $U_d = +40$ V indeed increases with increasing impact angle. The observed data represents the impact angle dependence of the total yield $\zeta = \delta + \eta$ and therefore is essentially a characteristic of the external secondary electron emission and backscattering processes. In case of negative dome

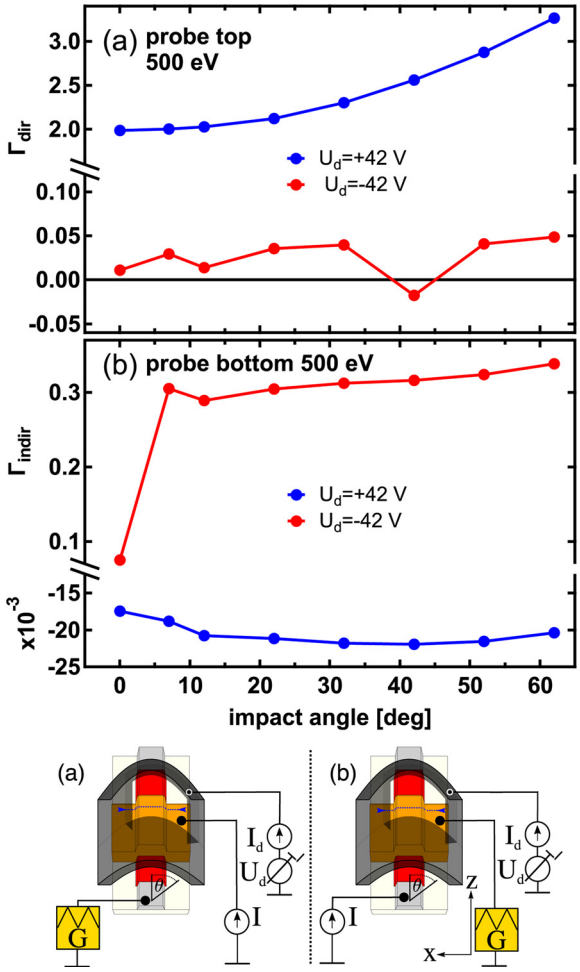

Fig. 10. *Direct* (a) and *indirect* (b) emission yields as defined in Eqs. (18 and 19) measured as a function of the impact angle (relative to the surface normal) for positive and negative dome voltage. The sample was irradiated in the center of the active area with 500 eV electrons. The values for each angle were obtained by *x*-scans. (For interpretation of the references to color in this figure legend, the reader is referred to the web version of this article.)

voltages, the yield is nearly zero and no clear impact angle dependence is observed (red circles in panel a).

The results of *indirect* experiments (see panel (b) of the Fig. 10) indicate an impact angle dependence of the yield for both polarities of the dome voltage, although the absolute values are much smaller at positive U_d. The yield Γ_{indir} measured for negative dome voltage reflects the absorption current, which strongly rises as soon as the irradiation is steered away from normal incidence, but afterwards shows only little variation with increasing impact angle. As explained above, the value of Γ_{indir} measured for positive U_d reflects the net internal emission current across the tunneling barrier. Since no external secondary or tertiary electrons re-enter the sample in this case, this quantity must be interpreted as a characteristic of the MIM device in connection with the electronic excitation generated in the top silver film by the primary electron impact. The finding of a decreasing internal emission yield with increasing projectile impact angle qualitatively resembles what was found for similar MIM devices under irradiation with Ar^+ ions [29–31].

Since the electrons generate electronic excitation in form of hot charge carriers (electrons and holes) along its path through the solid, the decrease of the junction current with increasing impact angle was interpreted in terms of the smaller penetration depth of the primary projectiles at oblique incidence, leading to the deposition of excitation energy closer to the surface and, hence, farther away from the buried tunnel junction.

3.5. Dome voltage dependence

In order to investigate the influence of the external field in more detail, measurements with varying dome voltage U_d were performed at a fixed irradiated spot on the active area.

This kind of measurement actually probes the energy of the emitted electrons and therefore provides valuable information regarding the secondary emission process. By changing the dome voltage U_d, the electric field between sample and dome is modified. By increasing the field strength, more and more electrons emitted from the sample are drained towards the dome electrode ($U_d > 0$ V) or reflected towards the sample ($U_d < 0$ V). The mechanism is similar to the influence of electrostatic forces on illuminated metals [33,34]. Therefore the dome voltage dependence of the measured currents is a tool for the study of external electrons.

3.5.1. Direct experiments

The *direct* emission yield Γ_{dir} measured as a function of the dome voltage U_d (solid lines) along with the dome current (dotted lines) is displayed in Fig. 11 for different kinetic energies. The impact point used for the red curve was located at the crossing position between *x* - and *z*-scans. This position was chosen because it is close to the center of the active area and thereby also in the center of the dome electrode. This area is also the most contaminated area of the top electrode, this might cause some problems especially in *direct* experiments which will be later discussed.

The *direct* yield adopts values in the range from 0.1 to +1.5 (up to +1.8 for 100 eV) and shows a characteristic dome voltage dependence. The most significant change of the signal can be observed in the range $-15 < U_d < +7$ V, for dome voltages above or below these values the slope of the yield is small, indicating that nearly all electrons are either pulled to the dome or reflected towards the sample. The upper and lower limit of −40 V and +40 V, as applied in this work, therefore do not affect the validity of the findings since a higher dome voltage would not significantly change the results. For comparison, the current measured on the dome electrode is also displayed in Fig. 11 as dashed lines. The values of this current measured for negative dome voltage are negative, indicating that electrons effectively leave the dome electrode under these conditions. Looking at the data presented in Fig. 11, it is obvious that both Γ_{dir} and I_{dome} react on the dome voltage in a similar way, but the two curves are not identical. At positive values of U_d, both curves show a positive slope and approach a plateau at similar values for $U_d > 20$ V. At negative dome voltage, on the other hand, both Γ_{dir} and I_{dome} strongly decay and appear to approach a plateau each at different values.

For a positive dome voltage, secondary electrons emitted from the irradiated sample are steered towards the dome, since the cylinder like shape of the dome electrode efficiently samples most of the electrons emitted from the irradiated surface regardless of their emission angle and energy. Two mechanisms for a positive dome voltage are possible:

- The negative space charge generated by the emitted low energy secondary electrons by themselves is dissolved. Increasing the positive value of U_d therefore leads to a higher fraction of secondary electrons reaching the dome electrode.
- At the same time, the emission of tertiary electrons from the dome electrode becomes more and more suppressed, since these electrons must overcome the increasing decelerating field in order to reach the sample surface.

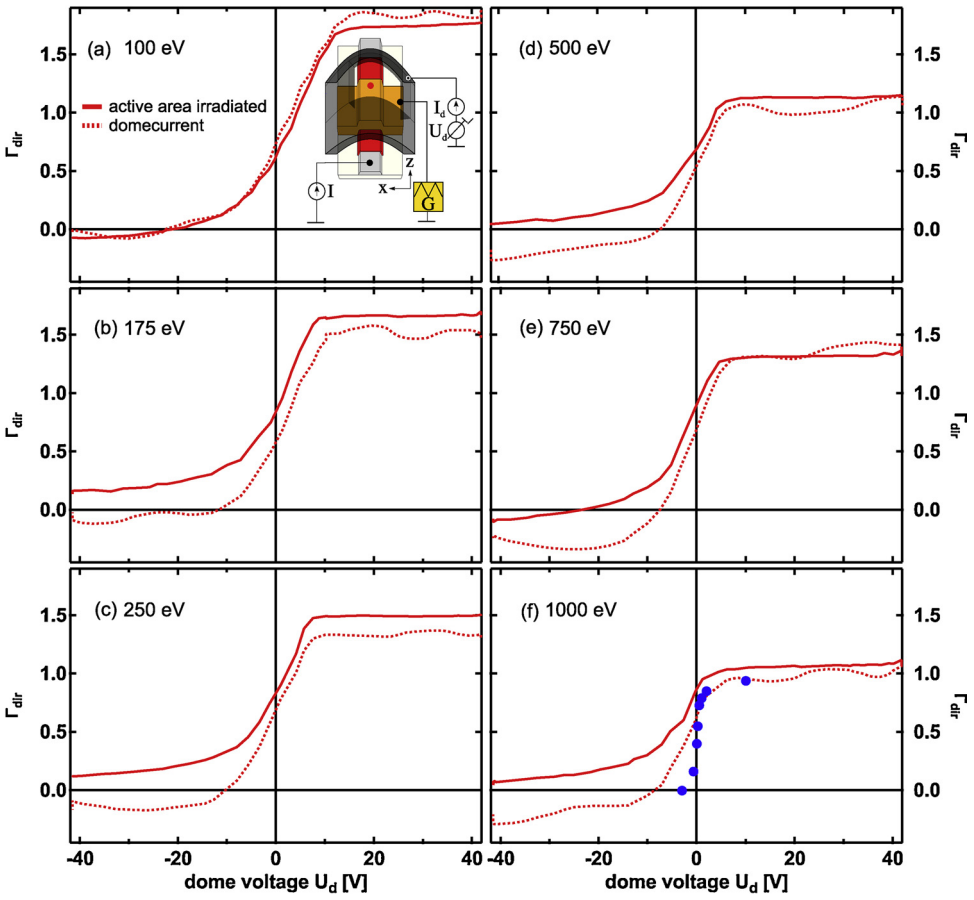

Fig. 11. Dome voltage dependence of Γ_{dir}. Overview of *direct* experiments for different energies in the center of the active area (red circle in inset of panel a) of the MIM. Solid lines: Γ_{dir}. Dotted lines: Dome current measured simultaneously on the dome electrode and scaled to 1 when $I_{dome} = I_{prim}$. Blue circles in panel (f): Voltage dependence of the normalized photocurrent from a carbon arc illuminated metal surface [32]. (For interpretation of the references to color in this figure legend, the reader is referred to the web version of this article.)

Obviously, a value of $U_d = +10$ V is sufficient to keep practically all low energy tertiary electrons from leaving the dome surface. In that case secondary and backscattered electrons leaving the irradiated silver surface contribute to the measured *direct* emission yield Γ_{dir}; all electrons reaching the dome electrode constitute the measure dome current I_{dome}.

Therefore, both quantities provide comparable information and approach the value of the total emission yield ζ, as seen in Fig. 15. The slight differences between both curves observed at higher impact energies can be interpreted as a small part of the backscattered electrons escaping through the slit. These electrons are therefore not collected by the dome electrode. Moreover, the elastic backscattering of high energy electrons impinging onto the dome electrode will lead to a reduction of the measured dome current.

For a negative dome voltage, on the other hand, a significant fraction of the secondary electrons emitted from the irradiated sample surface with energies above $E_{max} = |e \cdot U_d|$ are prevented from reaching the dome, while all tertiary electrons are extracted away from the dome electrode. In that case, the measured dome current must eventually become constant at a value given by the difference between incoming backscattered electron current I_{bse} and leaving tertiary current I_{tde}. Normalized to the primary electron current, the measured value should approach the quantity $\eta \cdot (1 - \delta_{dome})$ as explained above in Eq. (16). A negative value is justified by a tertiary emission yield δ_{dome} at the dome electrode larger than unity for all impact energies above 100 eV.

The secondary electrons repelled away from the dome and, in particular, the tertiary electrons emitted from the dome surface do not necessarily end up in the irradiated electrode of the MIM sample. Depending on the field configuration as well as its emission energy and angle, a reflected secondary electron or a tertiary electron emitted from the dome surface might also impinge onto other parts of the grounded sample (holder). Thereby $I < I +$ prim and the measured value of Γ_{dir} stays above zero (see Eq. (18)). As a consequence, the corresponding curve of the Yield resides above the normalized dome current curve in this regime.

The results obtained at $U_d = 0$ V can be compared with our previous measurements without the dome electrode [17]. The data presented here, however, clearly show that even small external fields arising, for instance, from space charge effects generated by the primary or secondary electrons may significantly influence the signal. In combination with the overlap between deceleration of secondary electrons (for $U_d < 0$ V) and tertiary electrons (for $U_d > 0$ V), this makes a quantitative interpretation of the measured curves in terms of the energy distribution of the emitted electrons difficult.

But one should mention that the observed dome voltage dependence of the yield Γ_{dir} can be well compared with early works on the voltage dependence of the photoyield. We chose table 5 of Lenard's work [32] because the distance of the counterelectrode to the illuminated metal surface was 1 cm in that work; this is pretty similiar to the mean distance of our dome electrode to the electron irradiated silver top electrode in our work. Lenard's data are shown as blue circles in panel (f) of Fig. 11. The agreement of our values for $\Gamma_{dir}$to Lenard's data is good from 0 V to 10 V. There is a mismatch between the two data sets for negative dome voltage. This is due to the reflection of electrons by the dome electrode to parts of the sample (holder) which are not connected with the current measurement as mentioned above.

The voltage dependence of the yield Γ_{dir} turns out to be tightly connected with the impact point of the e-beam on the MIM device. Two impact points on the silver top electrode (see red point on the active area and blue point aside from the active area in the left pictogramm of Fig. 12) were chosen and the voltage dependencies measured in *probe top* mode which are shown in panels (a) and (b). These two data sets can be compared with an experiment in *probe bottom* mode; in this case the aluminium bottom electrode is irradiated at a position just above the

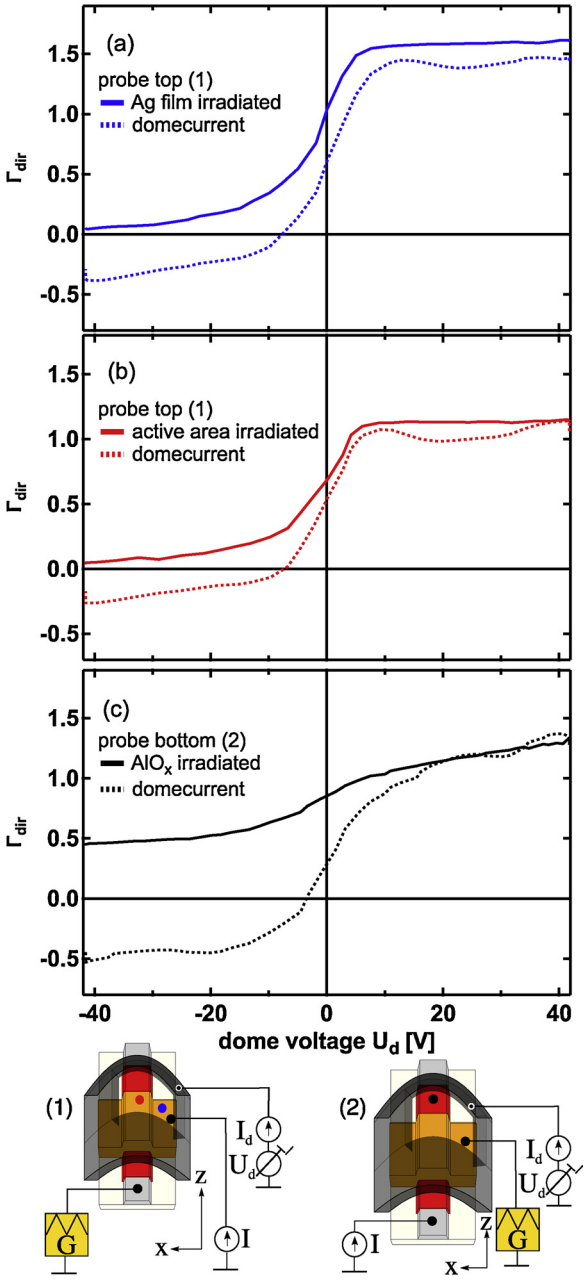

Fig. 12. *Direct* emission yield Γ_{dir} as calculated via Eq. (14) (solid lines) and measured dome current normalized to the primary electron current (dotted lines) vs. dome voltage U_d measured with 500 eV kinetic electron impact energies for: (a): irradiation of the silver film outside the active area (*probe top* mode); see blue dot in inset (1); (b): irradiation of the silver film within the active area (*probe top* mode): see red dot in inset (1); (c): irradiation of the oxide covered aluminum film (*probe bottom* mode): see black dot in inset (2). (For interpretation of the references to color in this figure legend, the reader is referred to the web version of this article.)

silver top electrode (see black circle in the right pictogramm). For all three experiments the impact energy is 500 eV. The saturation value of Γ_{dir} for $U_d > +20$ V is above 1.5 for the impact point aside from the active area (panel (a)). When the center of the active area is irradiated, the saturation value is ≈ 20% lower (≈1.1 see panel (b)). We attribute this finding to the carbon contamination in the center of the active area (the region with the longest irradiation time because the *x*- and *z*-scans cross). The contamination effectively reduces the secondary electron yield.

In panel (c), the direct experiment with the irradiation point on the bottom aluminum electrode is shown. The saturation value for positive dome voltages of ≈1.2 is close to the value for the experiment on the carbon contaminated silver surface in panel (b), but significant differences show up for negative dome voltages. The value for Γ_{dir} decreases only to values of 0.5 and not to values close to 0 as in panels (a) and (b). This means that $I \approx 0.5 \cdot I_{Prim}$, so half of the primary electrons are not moved back to the aluminum bottom electrode due to the negative dome electrode potential. This might be caused by

- the asymmetric shape of the dome electrode field at the edge of the slit
- the larger area of the silver electrode being able to recapture electrons released in the aluminum compared to the smaller area of the aluminum electrode being able to recapture electrons released in the silver top electrode.
- a fundamentally different emission spectrum of the oxide covered aluminum compared to the silver.
- a fundamentally different angle distribution of the emitted electrons due to the diffraction of the electron waves at the metal–oxide interface of the oxide covered aluminum electrode.

The two latter points might be affirmed by: (i) The overall comparable low influence of the dome voltage on Γ_{dir}. The derivative $d\Gamma_{dir}/dU_d$ is also very low for the aluminum/oxide system at $U_d = 0$. ii) The negative value of $I_{dome} = -0.5 \cdot I_{Prim}$ for the dome current at negative dome voltage also points to a very strong emission of tertiary electron from the dome electron towards the aluminum electrode for example enabled by a large fraction of high energy backscattered electrons from the oxide covered aluminum.

3.5.2. *Indirect experiments*

The dome voltage dependence of the *indirect* emission yield Γ_{indir} is shown in Fig. 13 for different primary electron impact energies. One important information obtained from these plots is that the measured values of Γ_{indir} become independent of U_d for dome voltages below −15 V.

For these negative value of U_d, the yield reflects the normalized absorption current I_{abs}, which contains contributions from cross-absorption of secondary electrons emitted from the irradiated surface as well as from absorption of tertiary electrons emitted from the dome electrode. These contributions apparently saturate already at relatively low external field strength. The energy dependence of the absorption current will be discussed in panel (c) of Fig. 14.

For positive values of U_d, the measured yield quickly drops to nearly zero for $U_d > +15$ V, reaching a plateau at very low values of Γ_{indir} which can be either positive or negative depending on the primary electron impact energy. In this regime, the (cross-)absorption current is effectively suppressed due to the attractive dome potential, and the measured *indirect* emission yield is therefore thought to consist of the real internal transport of excited charge carriers across the tunnel junction. The energy dependence of this real internal transport of charge carriers will be shown in panel (a) of Fig. 14.

For $U_d = 0$ V, the external field over the MIM system vanishes. These data will be compared with our previous work without dome electrode in [17]. The energy dependence of these data will be shown in panel (b) of Fig. 14.

The data displayed in panel (a) of Fig. 14 for $U_d > +15$ V are assigned to the true internal current across the tunnel junction, and the observed energy dependence must therefore arise from a different level of electronic excitation generated at different primary electron impact energy. Except for the lowest impact energy of 100 eV, the internal emission yield is negative, indicating that the contribution of holes (I_{int}^{h}) must overbalance that of excited electrons (I_{int}^{e}) to the total internal emission current I_{int}.

The values depicted in panel (b) of Fig. 14 for $U_d = 0$ V could in principle be compared to those measured in our previous experiments

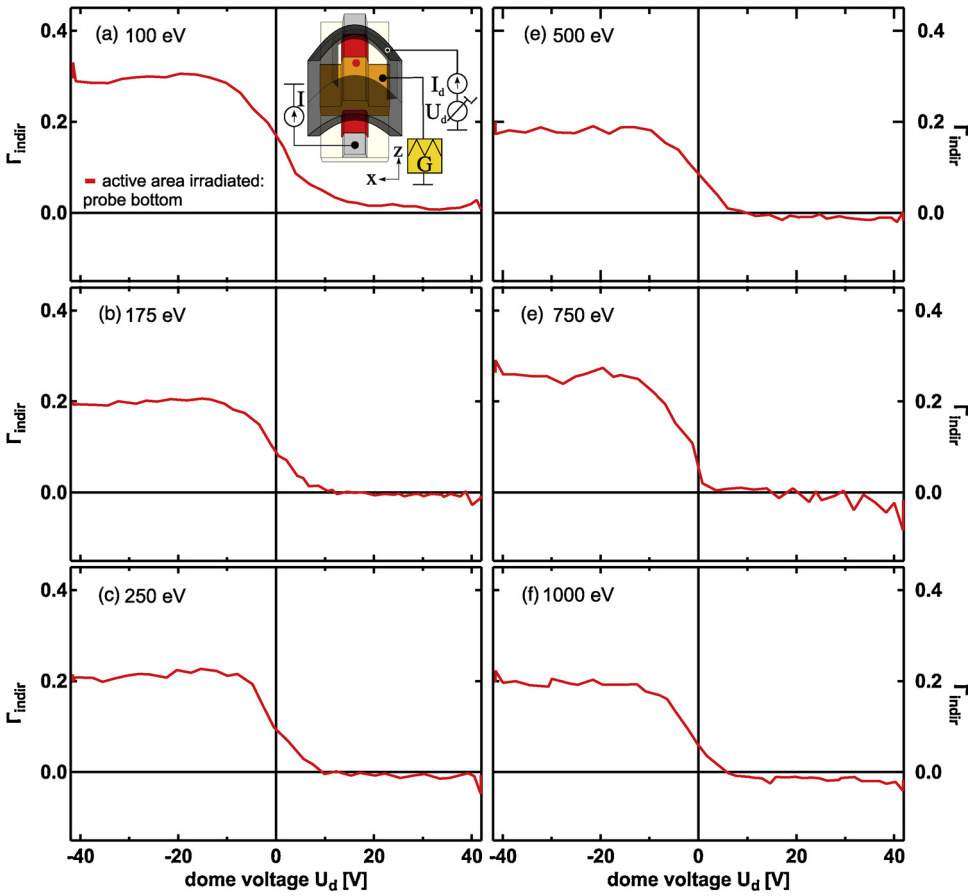

Fig. 13. Overview of *indirect* experiments where the active area is irradiated (red dot in inset) while the current is measured in the aluminum bottom electrode (*probe bottom* mode). The yield Γ_{indir} is calculated by the formula (19) and shown as a function of the dome voltage U_d for different kinetic energies from 100 eV (a) to 1000 eV (f). (For interpretation of the references to color in this figure legend, the reader is referred to the web version of this article.)

without the external dome electrode; values between 0.15 and 0.08 were shown in Figure 10 (b) of [17]. This is pretty similar to values of ≈0.1 in panel (b). Although the observed impact energy dependence appears very similar to that depicted in panel (a), one should note that the absolute values of Γ_{indir} are now positive, indicating a net electron flux into the aluminum bottom electrode.

The values Γ_{indir} measured at $U_d = 0$ V are comparable with that observed without the dome electrode; values between 0.15 and 0.08 were shown in Figure 10 (b) of [17]. Since no tertiary electrons were generated in that case, we conclude that the apparent "*internal*" emission yield measured in ref. [17] must be dominated by cross-absorption of low energy secondary electrons which are externally emitted from the irradiated silver electrode. In that context, it is of interest to ask how these electrons may be deflected back to the emitting surface. We suggest that this is caused by a negative space charge above the surface which is generated by the cloud of emitted low energy electrons themselves. A positive dome voltage then counteracts the effect of the space charge field, thereby reducing and eventually neutralizing its influence and leading to a saturated emission current towards the dome electrode in the same way as in a diode electron tube.

The data in panel (c) of of Fig. 14 for $U_d < -15$ V show the energy dependence of the absorption current. One can see that the strongest absorption current appears at 100 eV primary energy. Values for Γ_{indir} of 0.3 can be seen in the saturation of negative dome voltages. For higher primary energies lower values of $\Gamma_{indir} \approx 0.2$ are detected with one exception at 750 eV where again a value close to 0.3 appears. The high values of 0.3 for 100 eV can be justified to the low energy of emitted electrons. They can be very efficiently be directed to the aluminum electrode by the dome electric field. The exceptional strength of the absorption current at 750 eV cannot be justified in the moment.

In any case, the results obtained here clearly demonstrate that – at least for the electron irradiation experiments performed here – "*internal*" currents measured with nanostructured MIM devices as investigated here may be strongly influenced by *external* electric fields, and the implementation of measures suppressing possible external cross-absorption currents is necessary in order to arrive at meaningful results describing the true *internal* transport of excited charge carriers across the buried part of the oxide layer.

3.6. Evaluation of the total emission yield

From the experiments performed here, we can unambiguously extract the impact energy dependence of the total electron emission yield $\zeta = \eta + \delta$. As explained above, the value of ζ can be calculated as the difference between the *direct* and *indirect* emission yields measured with maximum positive dome voltage. Alternatively, this quantity should be equivalent to the normalized dome current measured under these conditions. In the following, we evaluate this quantity for irradiation of the top silver electrode of the MIM device. For that purpose, in principle three different sets of experimental data are available within this publication:

- position dependent *direct* and *indirect* emission yield measured at dome voltage U_d (x-scans in Figs. 5 and 6) and evaluated via Eq. (10).
- *direct* and *indirect* emission yield measured with variable dome voltage U_d at constant position of the irradiated spot (see Figs. 11 and 13) and evaluated via Eq. (10)
- dome current measured in *direct* and *indirect* experiments evaluated using Eq. (11)

Averaging the results obtained from all *direct* and *indirect* current measurements performed in this work, we arrive at the total emission yield values depicted in panel (b) of Fig. 15. For comparison, the results

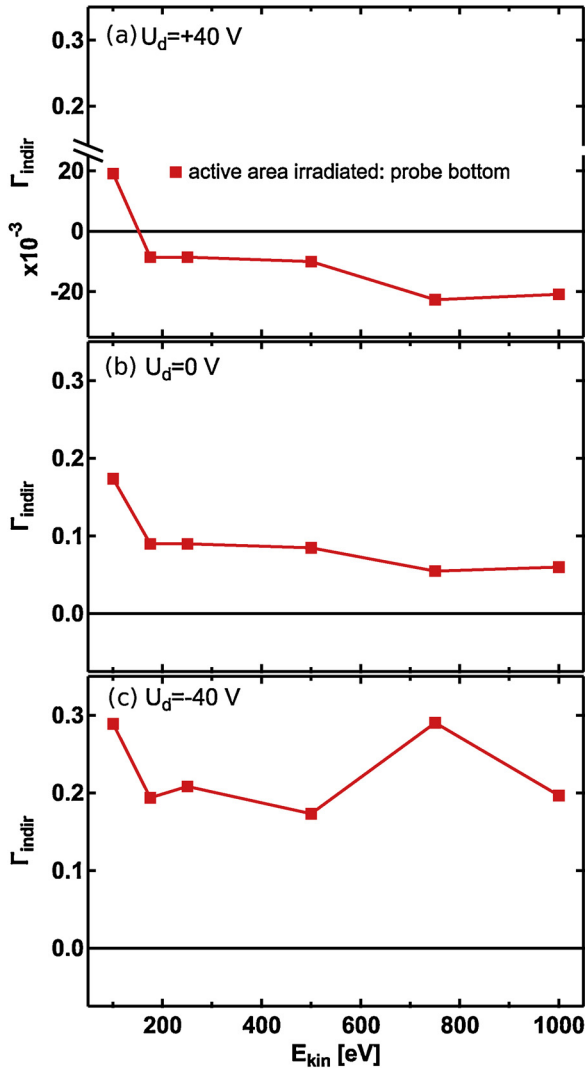

Fig. 14. Evaluation of *indirect* experiments as a function of the kinetic energy for different dome voltages: +40 V in (a), 0 V in (b) and −40 V in (c).

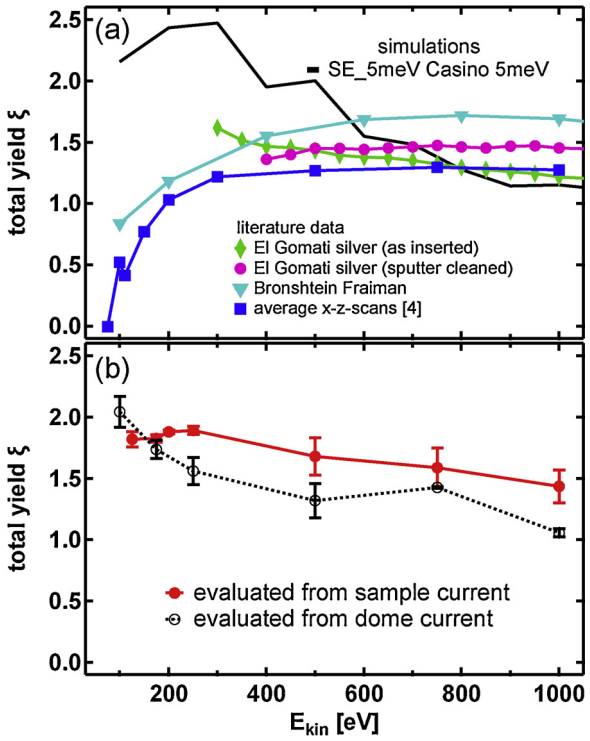

Fig. 15. (a): Total emission yield ζ as a function of the kinetic electron impact energy during irradiation of a silver film as reported in the literature obtained by summing η and δ: El Gomati from [35,36], Bronshtein Fraiman from [37] and average $x-z$-scans from [17] and calculated using Casino Monte Carlo for modified settings [39,17]. (b): experimental results from this publication obtained via evaluating I^{+}_{dome} (black curve) and obtained by evaluating the sample current via Eq. (10) (red curve), respectively. (For interpretation of the references to color in this figure legend, the reader is referred to the web version of this article.)

obtained from corresponding dome current measurements are also included in the figure. Both results largely agree within the statistical error and exhibit a falling trend with increasing primary electron impact energy, with the highest value of $\zeta \approx 1.8$ emitted electrons per impinging primary electron impact being measured for the lowest impact energy around 100 eV investigated here. The yield values determined from the measured dome current tend to slightly underestimate those determined from the measured sample current. This probably originates from elastic backscattering of high-energy electrons impinging onto the dome electrode surface. Since these electrons are not re-tended by the positive dome potential of +40 V, they escape from the dome surface, thereby reducing the measured electron current into the dome electrode. The yield values depicted in panel (b) of Fig. 15 can now be compared to available literature data on the secondary electron emission coefficient δ and the backscattering coefficient ζ. For a silver surface as investigated here, corresponding data sets covering the impact energy range studied here are available in refs. [35,36] and [37]. These data sets are of special interest here since η and δ were measured within the same experimental set-up. The total emission yield ζ calculated from these data are shown in panel (a) of Fig. 15, along with our previous experimental results obtained from sample current measurements without the dome electrode [17]. It is immediately evident that the data depicted in panels (a) and (b) do not coincide. For impact energies above approximately 400 eV, all three data sets displayed in panel (a) basically show an almost constant emission yield with values around $\zeta \approx 1.5$. Looking at the data published by El-Gomati and Walker [35,36], one finds different trends for a contaminated ("as inserted") and sputter cleaned silver surface. Since the MIM devices investigated here were analyzed without prior sputter cleaning the surface, our data should be compared to their "as inserted" data shown in panel (a), which in fact exhibits the same slightly falling trend with increasing impact energy as measured here. Unfortunately, their data does not cover the range of lower emission energies, where the discrepancy between panels (a) and (b) becomes more severe. The only data set which is available in this energy regime is that published by Bronshtein et al. [37], which shows a falling emission yield with decreasing impact energy between $\zeta \approx 1.7$ at 600 eV and $\zeta \approx 0.8$ at 100 eV. It should be noted that these data were measured under not well specified surface and vacuum conditions, although the work published by the same group reports experiments performed under well controlled surface and high vacuum conditions [38].

The strongest discrepancy observed in Fig. 15 is found with our own previously published data [17] measured on the same MIM device, which show a strongly decreasing emission yield with decreasing impact energy. In judging this difference, it is noteworthy that the data reported in ref. [17] were measured without the external dome electrode and therefore ζ was solely evaluated from the measured *direct* emission yield Γ_{dir} (termed Γ_{ext} in ref. [17]), thereby disregarding the possible re-absorption of emitted low energy secondary ions. On the other hand, the discussion in the preceding Section 3.5.2 clearly shows that the *indirect* emission yield Γ_{indir} (termed Γ_{int} in ref. [17]) measured in these experiments was significantly influenced by a non-negligible cross-absorption current. As a consequence, it appears reasonable to

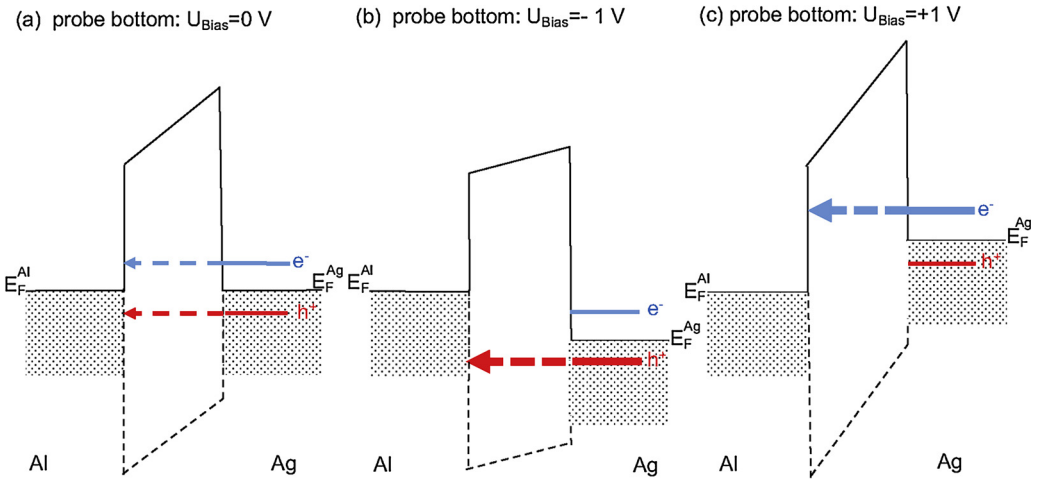

Fig. 16. (a): Energy levels in the MIM device under bias voltage with silver top electrode and aluminum bottom electrode. (b) A negative bias voltage on the bottom electrode acts as retarding field for excited electrons e^- in the top electrode and eases the transport of excited holes h^+. (c) A positive bias voltage on the bottom electrode acts as retarding field for excited holes in the top electrode and eases the transport of excited electrons.

assume an even larger re-absorption contribution to the measured direct current I_{dir}, which effectively reduces the apparent secondary electron yield. In conclusion, we therefore regard the results obtained here and displayed in panel (b) of Fig. 15 more reliable. This interpretation is corroborated by theoretical calculations using the Casino Monte-Carlo package [39], which are also included in panel (a) of Fig. 15. These calculations, which have been described in detail in ref. [17], reproduce our experimental finding of an overall decreasing emission yield in the impact energy range studied here quite well.

3.7. Bias voltage dependence

The specific influence of a bias voltage on the hole and electron transport can be explained by a bias-induced modification of the two-band tunnel barrier as sketched in Fig. 16. In case of 0 V bias (panel (a)) and excitation of the silver electrode, the internal current from the irradiated silver towards the non-irradiated aluminum electrode may consists of both e^- and h^+ currents with opposite polarity. By applying a bias voltage, the potential of the silver electrode is shifted up- or downwards with respect to that of the aluminum electrode. By convention, we define the polarity of the bias voltage such that a negative bias acts as a retarding field for the excited electrons and therefore decreases the electron current while simultaneously increasing the hole current crossing the tunneling barrier. For irradiation of the top silver film and the current measured in *probe bottom* mode, this situation is depicted in panel (b) of Fig. 16. The situation for a positive bias voltage is sketched in panel (c) where the bias now acts as a retarding field for excited holes, while the transport of excited electrons is eased.

In Section 3.5.2, it was shown that the measured *indirect* emission yield Γ_{indir} can be significantly influenced by an external electric field established by the dome electrode voltage U_d, and the results indicate that Γ_{indir} must contain an external emission mediated contribution where secondary electrons released from the irradiated silver electrode are absorbed in the current-metered aluminum electrode. In particular, the results were interpreted such that sufficiently positive values of U_d effectively suppress the cross-absorption current, leaving only the true internal current to be measured under these conditions. In this section, we therefore examine the dependence of Γ_{indir} measured under irradiation of the top silver film in connection with in a variable *internal* field in the device established by a bias voltage. Since the measurement was done in *probe bottom* mode, the current-metered aluminum electrode was kept fixed at ground potential, so that the bias voltage was applied to the irradiated silver electrode. In the convention described above, a positive potential on that electrode therefore corresponds to a negative bias voltage and vice versa.

As a result of such experiments, Fig. 17 shows the dome voltage dependence of the *indirect* emission yield Γ_{indir} as measured for different values of the bias voltage. It is immediately evident that the curves strongly react on the internal bias voltage. The overall shape remains the same, with a plateau at values around $\Gamma_{indir} \approx 0.3$ for $U_d < -15$ V, followed by a strong decay to nearly zero and a small slope for $U_d > +15$ V. The more or less constant value at sufficiently negative dome voltage reflects the absorption current I_{abs}, which obviously becomes slightly larger at positive bias voltage and drops by approximately 10% at a negative bias voltage of -1 V. Since a negative bias voltage corresponds to a positive potential of the irradiated silver electrode with respect to that of the bottom aluminum electrode, the cross-absorption current will be reduced, thereby reducing the value of the *indirect* emission yield. Alternatively, a positive bias voltage corresponds to a negative potential on the silver electrode, which will drive electrons away from that electrode and therefore increase the cross-absorption current.

For positive dome voltages the effect of the bias voltage is much weaker. In part (b) of Fig. 17 a zoom of the Γ_{indir} values between 0.015 and -0.015 is shown. The curves exhibit a residual falling slope towards higher U_d values, which is essentially the same for all measured curves regardless of the bias voltage. We attribute this slope to the further reduction of a remaining absorption current induced by tertiary electrons leaving the dome electrode with higher kinetic energy. The curves measured for different bias voltage run essentially parallel, so that the vertical shift must be interpreted as a bias-induced modification of the true internal emission current. The negative bias leads to a downward shift, while positive bias produces an upward shift of the internal yield. To interpret these results, we note again that the measured internal emission current results from a balance between transport of excited electrons and holes from the irradiated silver electrode to the underlying aluminum electrode. The small values for *indirect* emission yield do not necessarily imply negligible transport of excited charge carriers across the tunnel junction. If both contributions I_{int}^e and I_{int}^h were exactly identical, one would measure an internal emission current of zero, even if both contributions would have sizable values. At negative bias voltage, the transport of excited holes is increased with respect to that of the excited electrons, leading to a (more) negative *indirect* emission current. At positive bias, on the other hand, the transport of electrons is enhanced and that of holes is reduced, leading to a more positive value of the *indirect* emission current. As a consequence, we conclude that the effect of the bias voltage observed in Fig. 17 can be understood in terms of a modification of the internal carrier transport in the metal-insulator-metal system. For completeness, we note that repeated measurements at 0 V bias voltage do not lead to the same value of Γ_{indir}, as seen in Fig. 17. During the experiments, we found that the same values can again be reached when a bias voltage with opposite polarity is applied in between. We therefore assign this effect to a field induced change of the oxide barrier. Such dielectric

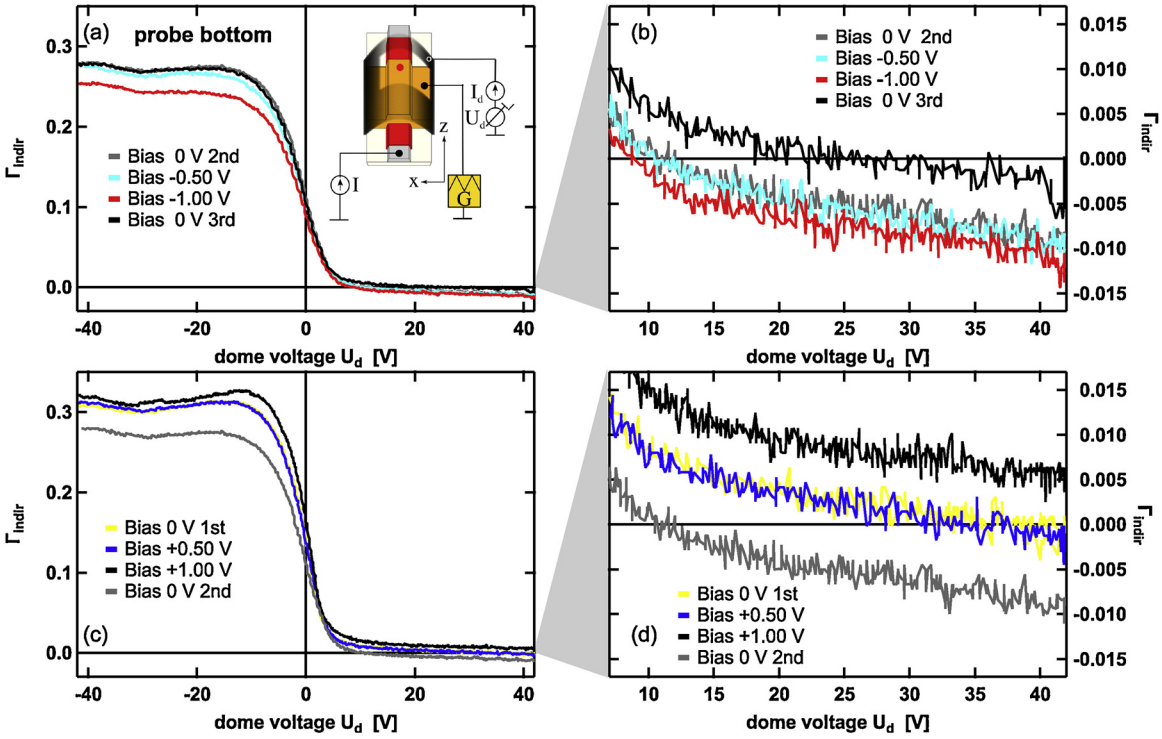

Fig. 17. Yield in the *probe bottom* mode as a function of the dome voltage for different static bias voltages taken under irradiation of the active area (red dot in inset) with 500 eV electrons. (a): Negative bias voltage. (b): Zoomed view of (a) of the negative dome voltage. (c): Positive bias voltage. (d): Zoomed view of (c) of the positive dome voltage. (For interpretation of the references to color in this figure legend, the reader is referred to the web version of this article.)

remanence effects are often found in thin oxide layers [23,40], and they are even more dominant in titanium oxide layers [12].

4. Conclusion

The experiments performed here demonstrate that the interpretation of excitation-induced "*internal*" currents measured in a metal-insulator-metal device may be complicated by re- and cross-absorption effects involving *external* electron emission from the irradiated surface. Especially under irradiation with an electron beam, low energy secondary electrons are emitted from the irradiated surface, which may be strongly influenced by weak external electric fields. We show that even under conditions where the space above the irradiated surface is nominally field-free (i.e. at a dome potential of 0 V with respect to the sample potential), part of the externally emitted electrons must be deflected back to the sample surface, thereby contributing to a re-absorption current into the irradiated *top* electrode along with a cross-absorption current into the exposed part of the second, non-irradiated *bottom* electrode. At the same time, energetic electrons backscattered from the irradiated surface may hit nearby electrodes, where they can either be backscattered again or release low energy tertiary electrons. All electrons leaving such a surface may end up in the sample again and also contribute to the (re)absorption current. Using a specially designed external "dome" electrode surrounding the irradiated MIM device, we demonstrate that these parasitic currents can be suppressed at sufficiently high positive dome potential, thereby permitting to determine the real *internal* emission current across the tunneling junction. For the electron bombardment conditions applied here, the experiments reveal that this *internal* emission current is much smaller than the apparent device current measured either without the dome electrode or with that electrode set to a more negative potential. Moreover, it is shown that depending on the excitation conditions (here: the electron impact energy and angle) the *internal* emission current exhibits a different variation compared to that of the *external* emission currents and even change its sign, reflecting a change from a dominating electron to a dominating defect electron (hole) transport. This interpretation is corroborated by experiments where a varying bias voltage is applied between the two MIM electrodes, thereby changing the transport characteristics of the two-band tunnelling junction.

Besides the identification of true *internal* emission currents generated by the primary electron impact, the experiments with an *external* dome electrode also allow an unambiguous determination of the total *external* emission yield ζ of secondary and backscattered electrons from the irradiated surface. This is of interest since there is only very few literature data available for this quantity in the low impact energy range studied here. For impact energies above approximately 400 eV, our measurements performed under irradiation of the top silver MIM electrode show reasonable agreement with available literature data measured for a (contaminated) silver target surface, including our own previous data which was measured on a similar MIM system as investigated here. A qualitative discrepancy, however, is found at lower impact energies, where the experiments performed here deliver the highest emission yields at the lowest investigated energies of 100 eV to 200 eV, followed by a continuously falling trend with increasing impact energy. This result contradicts our previous data, which was measured without the *external* dome electrode and showed a strongly falling emission yield with decreasing impact energy. This finding clearly demonstrates the important role of an *external* field in order to overcome possible re-absorption of the emitted low energy secondary electrons induced, for instance, by a space charge cloud above the irradiated surface.

The results also reveal that carbon contamination is an issue in the experiments discussed here, which significantly modifies the *external* emission behavior of the sample surface. The buildup of such contamination is a frequent issue during electron irradiation of metallic surfaces [41], where it may for instance arise from electron induced fragmentation of adsorbed carbon species. The amount of carbon deposited at the irradiated surface increases with increasing electron fluence, making the contamination worse at sample areas which are more frequently irradiated. In the context of the present experiments,

this leads to a position dependent modification of particularly the signal measured in direct experiments when irradiating different spots on the investigated MIM device. These effects explain the difference between some of the results obtained in position dependent experiments where the primary electron beam was scanned across the MIM surface at a fixed dome voltage on one hand and U_d-dependent experiments where the dome voltage was scanned under irradiation of a constant surface position on the other hand.

Acknowledgements

The authors are greatly indebted to the “Deutsche Forschungsgemeinschaft (DFG)” for funding part of this work in the framework of the collaborative research centers SFB 616 (TP A3 and A4) and SFB 1242 (TP C05). We also thank Hermann Nienhaus for valuable discussions.

References

[1] P.W. Hawkes, Sir Charles Oatley and the scanning electron microscope, Adv. Imaging Electron Phys. 133 (2004).
[2] T.E. Everhart, Simple theory concerning the reflection of electrons from solids, J. Appl. Phys. 31 (1960) 1483–1490.
[3] T.E. Everhart, R.F.M. Thornley, Wide-band detector for micro-microampere low-energy electron currents, J. Sci. Instrum. 37 (1960) 246.
[4] S. Meyer, C. Heuser, D. Diesing, A. Wucher, Kinetic electronic excitation of solids by fast-particle bombardment, Phys. Rev. B 78 (2008) 035428.
[5] G. Carter, J.S. Colligon, J.H. Leck, Ion sorption in the presence of sputtering, Proc. Phys. Soc. 79 (1962) 299.
[6] B. Szapiro, J.J. Rocca, Electron emission from glow – discharge cathode materials due to neon and argon ion bombardment, J. Appl. Phys. 65 (1989) 3713–3716.
[7] D.A. Kovacs, A. Golczewski, G. Kowarik, F. Aumayr, D. Diesing, Low-energy ion-induced electron emission in metal-insulator-metal sandwich structures, Phys. Rev. B 81 (2010).
[8] A. Duvenbeck, B. Weidtmann, O. Weingart, A. Wucher, Modeling hot-electron generation induced by electron promotion in atomic collision cascades in metals, Phys. Rev. B 77 (2008) 245444.
[9] S. Meyer, D. Diesing, A. Wucher, Kinetic electron excitation in atomic collision cascades, Phys. Rev. Lett. 93 (2004) 137601.
[10] B. Mildner, E. Hasselbrink, D. Diesing, Electronic excitations induced by surface reactions of h and d on gold, Chem. Phys. Lett. 432 (2006) 133.
[11] D. Differt, W. Pfeiffer, D. Diesing, Scanning internal photoemission microscopy for the identification of hot carrier transport mechanisms, Appl. Phys. Lett. 101 (2012) 111608–111614.
[12] K. Stella, D.A. Kovacs, D. Diesing, W. Brezna, J. Smoliner, Charge transport through thin amorphous titanium and tantalum oxide layers, J. Electrochem. Soc. 158 (2011) P65–P74.
[13] D. Diesing, M. Merschdorf, A. Thon, W. Pfeiffer, Identification of multiphoton induced photocurrents in metal-insulator-metal junctions, Appl. Phys. B 78 (2004) 443–446.
[14] D.A. Kovacs, T. Peters, C. Haake, M. Schleberger, A. Wucher, A. Golczewski, F. Aumayr, D. Diesing, Potential electron emission induced by multiply charged ions in thin film tunnel junctions, Phys. Rev. B 77 (2008) 245432.
[15] T. Peters, C. Haake, D. Diesing, D.A. Kovacs, A. Golczewski, G. Kowarik, F. Aumayr, A. Wucher, M. Schleberger, Hot electrons induced by slow multiply charged ions, New J. Phys. 10 (2008) 073019.
[16] D. Diesing, D.A. Kovacs, K. Stella, C. Heuser, Characterization of atom and ion-induced “internal” electron emission by thin film tunnel junctions, Nucl. Instrum. Methods Phys. Res. Sect. B: Beam Interact. Mater. Atoms 269 (2011) 1185.
[17] M. Marpe, A. Wucher, D. Diesing, Transport of 75-1000 ev electrons in metal-insulator-metal devices, J. Electron Spectrosc. Relat. Phenomena 223 (2018) 37–52.
[18] L. Reimer, Scanning Electron Microscopy: Physics of Image Formation and Microanalysis vol. 45, Springer, 2013.
[19] K. Stella, S. Franzka, D. Bürstel, D. Diesing, D. Mayer, V. Roddatis, Electrochemical oxidation as vertical structuring tool for ultrathin ($d < 10$ nm) valve metal films, ECS J. Solid State Sci. Technol. 3 (2014) P143–P148.
[20] L. Reimer, Image Formation in Low-Voltage Scanning Electron Microscopy, Electron Optics, SPIE-The International Society for Optical Engineering, 1993, pp. 98–99.
[21] D. Diesing, A.W. Hassel, M.M. Lohrengel, Aluminium oxide tunnel junctions: influence of preparation technique, sample geometry and oxide thickness, Thin Solid Films 342 (1999) 282–290.
[22] A.W. Hassel, D. Diesing, Breakdown of ultrathin anodic valve metal oxide films in metal-insulator-metal-contacts compared with metal-insulator-electrolyte contacts, Thin Solid Films 414 (2002) 296–303.
[23] A.W. Hassel, D. Diesing, Trapping of transient processes in aluminium oxide thin films in a voltage pulse experiment, Electrochem. Commun. 4 (2002) 1.
[24] L. Malter, Thin film field emission, Phys. Rev. 50 (1936) 48–58.
[25] V.K. Agarwala, T. Fort, Effect of pressure and temperature on changes in the work function of aluminum during interaction with oxygen, Surf. Sci. 48 (1975) 527–536.
[26] P.M. Schneider, W.B. Fowler, Band structure and optical properties of silicon dioxide, Phys. Rev. Lett. 36 (1976) 425–428.
[27] B. Ealet, M. Elyakhloufi, E. Gillet, M. Ricci, Electronic and crystallographic structure of – alumina thin films, Thin Solid Films 250 (1994) 92–100.
[28] S. Meyer, C. Heuser, D. Diesing, A. Wucher, Kinetic electronic excitation of solids by fast-particle bombardment, Phys. Rev. B 78 (2008) 035428.
[29] C. Heuser, M. Marpe, D. Diesing, A. Wucher, Kinetic excitation of solids induced by energetic particle bombardment: influence of impact angle, Nucl. Instrum. Methods Phys. Res. Sect. B: Beam Interact. Mater. Atoms 267 (2009) 601–604.
[30] C. Heuser, M. Marpe, D. Diesing, A. Wucher, The possible role of anisotropy in kinetic electronic excitation of solids by particle bombardment, Nucl. Instrum. Methods Phys. Res. Sect. B: Beam Interact. Mater. Atoms 269 (2011) 1190–1194.
[31] M. Marpe, C. Heuser, D. Diesing, A. Wucher, Internal electron emission in metal-insulator- metal thin film tunnel devices bombarded with kev argon and gold-cluster projectiles, Nucl. Instrum. Methods Phys. Res. Sect. B: Beam Interact. Mater. Atoms 269 (2011) 972–976.
[32] P. Lenard, Über die lichtelektrische Wirkung, Ann. Phys. 313 (1902) 149–198.
[33] W. Hallwachs, Über den Zusammenhang des Electricitätsverlustes durch Beleuchtung mit der Lichtabsorption, Ann. Phys. 273 (1889) 666–675.
[34] W. Hallwachs, Über den E influss des Lichtes auf electrostatisch geladene Körper, Ann. Phys. 269 (1888) 301–312.
[35] M.M. El-Gomati, C.G.H. Walker, A.M.D. Assa’d, M. Zadrazil, Theory experiment comparison of the electron backscattering factor from solids at low electron energy (250-5000 ev), Scanning 30 (2008) 2–15.
[36] C.G. Walker, M.M. El-Gomati, A.M.D. Assa’d, M. Zadrazil, The secondary electron emission yield for 24 solid elements excited by primary electrons in the range 250-5000 ev: a theory/experiment comparison, Scanning 30 (2008) 365–380.
[37] I. Bronshtein, B.S. Fraiman, Vtorichnaya Elektronnaya Emissiya(Secondary Electron Emission), (1969).
[38] R. Bronshtein, I.M. Segal, Inelastic scattering of electrons and secondary-electron emission in certain metals I, Soviet Phys. Solid State 1 (1960) 1365–1496.
[39] H. Demers, N. Poirier-Demers, A. Réal Couture, D. Joly, M. Guilmain, N. de Jonge, D. Drouin, Casino Monte Carlo Software, (2016) http://www.gel.usherbrooke.ca/casino/index.html.
[40] M. Lohrengel, Thin anodic oxide layers on aluminium and other valve metals: high field regime, Mater. Sci. Eng.: R: Rep. 11 (1993) 243–294.
[41] D. Briggs, M. Shea, Practical Surface Analysis Auger and X-rays vol. 1, (1988).